Back action in quantum electro-optic sampling of electromagnetic vacuum fluctuations

T. L. M. Guedes [1] I. Vakulchyk,[2,3] D. V. Seletskiy,[4] A. Leitenstorfer [1] A. S. Moskalenko [5,*] and Guido Burkard [1,†]

[1]*Department of Physics and Center for Applied Photonics, University of Konstanz, D-78457 Konstanz, Germany*
[2]*Center for Theoretical Physics of Complex Systems, Institute for Basic Science (IBS), Daejeon 34126, Republic of Korea*
[3]*Basic Science Program, Korea University of Science and Technology (UST), Daejeon, Korea 34113, Republic of Korea*
[4]*Department of Engineering Physics, Polytechnique Montréal, Montréal, QC, Canada H3T 1J4*
[5]*Department of Physics, KAIST, Daejeon 34141, Republic of Korea*

The influence of measurement back action on electro-optic sampling of electromagnetic quantum fluctuations is investigated. Based on a cascaded treatment of the nonlinear interaction between a near-infrared coherent probe and the mid-infrared vacuum, we account for the generated electric-field contributions that lead to detectable back action. Specifically, we theoretically address two realistic setups, exploiting one or two probe beams for the nonlinear interaction with the quantum vacuum, respectively. The setup parameters at which back action starts to considerably contaminate the measured noise profiles are determined. We find that back action starts to detrimentally affect the signal once the fluctuations due to the coupling to the mid-infrared vacuum become comparable to the base shot noise. Due to the vacuum fluctuations entering at the beam splitter, the shot noise of two incoming probe pulses in different channels is uncorrelated. Therefore, even when the base shot noise dominates the output of the experiment, it does not contribute to the correlation signal itself. However, we find that further contributions due to nonlinear shot-noise enhancement are still present. Ultimately, a regime in which electro-optic sampling of quantum fields can be considered as effectively back-action free is found.

I. INTRODUCTION

When performing quantum measurements, the interaction with the measurement device typically causes a perturbation of the quantum state [1–5]. Even for experiments keeping the product of related uncertainties at their minimum, improving the accuracy with which one observable is measured inevitably increases the fluctuations in its canonically conjugate observable. This influence of the measurement device on a quantum system is called quantum back action (BA) [6]. Often, the BA is undesired, but in some cases it underlies the functionality of quantum-information processing schemes [7,8].

Fluctuations in noncommuting observables persist even when the system reaches its ground state. In recent years, remarkable experiments have probed the zero-point fluctuations of a plethora of quantum systems, in particular, single-mode mesoscopic mechanical resonators [9] and multimode electromagnetic radiation [10–12]. Theoretical and experimental evidence [13,14] points towards the inevitable presence of BA in quantum mechanical resonators probed by light in optical

*moskalenko@kaist.ac.kr
†guido.burkard@uni-konstanz.de

cavities. While the light affects the resonator through radiation pressure (Stokes and anti-Stokes scattering), the resonator imprints its phase-space signature on the photons in the cavity or, correspondingly, shifts the resonance frequency of the cavity [15]. This BA, however, can be avoided by coupling the vibrational modes of two oscillators through the cavity photons, allowing the BA contributions from the two modes to cancel each other [16].

Related arguments about mode coupling through BA were invoked to explain electro-optic (EO) measurements of correlations in the electromagnetic vacuum state [17]. The potential effect of BA in such experiments, however, might considerably diverge from those seen in optomechanical cavities [18,19] since the characteristic nonlinearity of the EO interaction effectively couples optical modes between and within channels, each of them consisting of an infinite and continuous set of modes. The potential of this advanced scheme spans from the exploration of Hawking/Unruh effects [20–23] to ultrafast quantum spectroscopy [24,25], thus calling for a formal and thorough description of the underlying physics.

In this paper, we theoretically study the BA in two experimental settings involving EO sampling of the electromagnetic ground state [10,17]. These measurements rely on a coupling that imprints information about a multimode quantum state on the ellipticity of a subcycle coherent pulse in a higher-frequency range. For a single-channel experiment [10] [see Fig. 1(b)], the interplay between shot noise (SN) and BA plays a crucial role in determining the optimal range of parameters. The situation is more complex when a second channel is
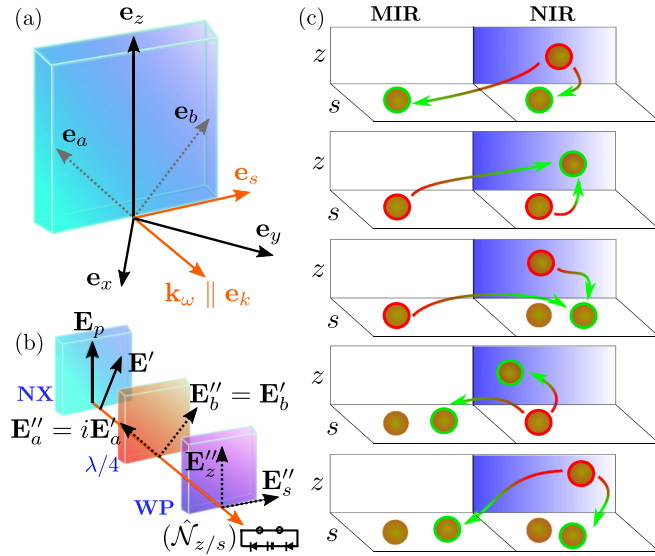
FIG. 1. (a) Nonlinear crystal (NX) and field components. The probe $\mathbf{E}_p$ is polarized along $\mathbf{e}_z$ and propagates with wave vector $\mathbf{k}_\omega = k_\omega \mathbf{e}_k$. The tensor components of the nonlinear susceptibility are such that only field components along $\mathbf{e}_x$ and $\mathbf{e}_y$ can mix with the probe, generating a new propagating quantum-field component along $\mathbf{e}_s$. (b) Scheme of an EO measurement. $\mathbf{E}_p$ changes its ellipticity in the NX due to the nonlinearly generated $\mathbf{e}_s$-polarized field component, resulting in $\mathbf{E}'$. A quarter-wave plate ($\lambda/4$) shifts the phase of the $\mathbf{e}_a$ component of $\mathbf{E}'$ by $\pi/2$, leading to $\mathbf{E}''$, which has its E_z'' and E_s'' components spatially split by a Wollaston prism (WP) before independent photon counting. (c) Illustration of the state evolution under the nonlinear interaction (cf. Appendix G). The states include z and s polarizations (in-plane and out-of-plane panels) and two frequency bands, MIR and NIR (left and right panels), with the z-polarized NIR coherent probe represented as a blue pool of photons. Red (green) contours represent annihilation (creation) of photons (golden spheres) and the arrows show the directions of the energy transfers. The first diagram (uppermost) shows the lowest-order perturbation of the initial state, with s-polarized MIR and NIR photons being created through annihilation of a probe photon. The second and third diagrams show the second-order processes that lead to no BA in the MIR (photons created by the first-order process are annihilated). The last two diagrams show the remaining second-order processes, which cause additional BA in the MIR via generation of extra photons.

included in the setup [17,26] as shown in Fig. 3(a). Here, the contribution of the base SN to the signal correlation drops out when averaging over many readout events [27]. We propose the working regimes most suitable to avoid undesired BA contributions to the EO signals (so that the measurement is considered effectively BA free) and explain the subtle (yet fundamental) role that the population of the measured modes plays not only in the data presented in Ref. [17], but also in the general conceptual understanding of quantum EO sampling.

II. SINGLE-CHANNEL MODEL

We start with a derivation of the cascaded contributions to the quantum electric field that build up within the nonlinear medium and proceed to their conversion into the EO signal noise upon detection. We initially consider a single-channel setup as sketched in Figs. 1(a) and 1(b). An incoming near-infrared (NIR) ultrashort probe pulse copropagates with a mid-infrared (MIR) vacuum-state electric-field component along the $\mathbf{e}_k = [110]$ axis of a zinc-blende-type nonlinear crystal (NX), as in Ref. [28]. The wave vector $\mathbf{k}_\omega = k_\omega \mathbf{e}_k$ of the probe pulse is perpendicular to the z axis of the crystal, which in turn is parallel to the probe electric field $\mathbf{E}_p = E_p \mathbf{e}_z$. Since the probe pulse is in a coherent state, we can write its field operator as $\hat{\mathbf{E}}_p(\mathbf{r}, t) = E_p(\mathbf{r}, t)\mathbf{e}_z + \delta\hat{\mathbf{E}}(\mathbf{r}, t)$, with $\delta\hat{\mathbf{E}}(\mathbf{r}, t)$ describing the (zero-point) quantum fluctuations. The (cascaded) contribution to the second-order nonlinear polarization arising in the crystal from the mixing between the probe and any s-polarized (with $\mathbf{e}_s = \mathbf{e}_z \times \mathbf{e}_k$) quantum-field contribution $\hat{E}_s^{(m)}$ present in the crystal is given by $\hat{\mathbf{P}}_m^{(2)}(\mathbf{r}, t) = -\epsilon_0 d\hat{E}_s^{(m)}(\mathbf{r}, t)E_p(\mathbf{r}, t)\mathbf{e}_s$. Here, ϵ_0 is the vacuum permittivity and $d = -n^4 r_{41}$ is the effective nonlinear susceptibility of the NX, with n being its refractive index (RI) at the center frequency of the probe and r_{41} its relevant EO coefficient [29]. The index m represents the number of cascaded steps generating a given contribution.

We divide the frequency domain into two segments, the MIR, represented by Ω, and the NIR, represented by ω, both of which can be expressed by $\Lambda \in \{\Omega, \omega\}$. The electric-field operator is given in its paraxial form [30,31] $\hat{\mathbf{E}}(\mathbf{r}, t) = \sum_{\sigma l p} \int d\Lambda \, \mathbf{e}_\sigma e^{i\Lambda(n_\Lambda r_k/c_0 - t)}\hat{E}_{\sigma l p}(\mathbf{r}, \Lambda)$, where

$$\hat{E}_{\sigma l p}(\mathbf{r}, \Lambda) = i\,\mathrm{sgn}(\Lambda)\sqrt{\frac{\hbar|\Lambda|}{4\pi\epsilon_0 n_\Lambda c_0}}\mathrm{LG}_{lp}(\mathbf{r}_\perp, \Delta r_k; \Lambda)\hat{a}_{\sigma l p}(\Lambda),$$

(1)

with amplitude distributions in the transversal plane located at $r_k = \mathbf{r} \cdot \mathbf{e}_k$ given by the Laguerre-Gaussian (LG) modes $\mathrm{LG}_{lp}(\mathbf{r}_\perp, \Delta r_k = r_k - L/2; \Lambda)$ with $\mathbf{r}_\perp = r_z \mathbf{e}_z + r_s \mathbf{e}_s$. The operator $\hat{a}_{\sigma l p}(\Lambda > 0) = \hat{a}_{\sigma l p}^\dagger(-\Lambda)$ [20,31] annihilates a photon with frequency Λ, polarization $\sigma = s, z$, and azimuthal l and radial p indices labeling the LG modes. Here, c_0 and n_Λ are the speed of light and the frequency-dependent RI of the NX, respectively. We assume an NX extended from $r_k = 0$ to L, so that the narrowest amplitude distribution for the LG modes occurs at the center of the crystal, $r_k = L/2$, where the waist of the mode profiles reaches its minimal value w_0. E_p is given by Eq. (1) with $\hat{a}_{\sigma l p}(\omega) \to \alpha_{\sigma l p}(\omega)$, and we assume its transversal profile to be in the fundamental mode, given by $g_{00}(\mathbf{r}_\perp) \equiv \mathrm{LG}_{00}(\mathbf{r}_\perp, 0; \omega) = \sqrt{2/\pi}\, w_0^{-1} \exp(-r_\perp^2/w_0^2)$ and $\alpha_p(\omega) \equiv \alpha_{z00}(\omega)$. For the remainder of this work, we shall exploit the fact that the NX is thin ($L \ll n_\Lambda \Lambda w_0^2/2c_0$) and consider all fields at $r_k = L/2$: $\hat{E}_{\sigma l p}(\{r_k = L/2, \mathbf{r}_\perp\}, \Lambda) \equiv \hat{E}_{\sigma l p}(\mathbf{r}_\perp, \Lambda)$. The indices l and p will be omitted whenever possible.

The nonlinear polarization acts as a source for the generation of multimode squeezed electric-field components [20–22] with polarization perpendicular to the probe. Neglecting the depletion of the probe, the NIR output field $\hat{\mathbf{E}}'$ is given by the input probe pulse plus the perturbative solutions to the wave equation sourced by each of the cascaded $\mathbf{P}_m^{(2)}(\omega)$ [27] (cf. [29] Sec. 1.6 and Chap. 2),

$$\hat{E}_s^{(m+1)}(\mathbf{r}_\perp, \omega) = \int_{-\infty}^\infty d\Omega\, \hat{E}_s^{(m)}(\mathbf{r}_\perp, \Omega)E_p(\mathbf{r}_\perp, \omega - \Omega)\zeta_{\omega,\Omega},$$

(2)

where $\hat{E}_s^{(1)}(\Omega) \equiv \delta\hat{E}_s(\Omega)$ represents the vacuum electric field in the MIR and $\hat{E}_s^{(m)}(\Omega)$ for $m > 1$ reads

$$\hat{E}_s^{(m)}(\mathbf{r}_\perp, \Omega) = \int_{-\infty}^{\infty} d\omega \, \hat{E}_s^{(m-1)}(\mathbf{r}_\perp, \omega) E_p^*(\mathbf{r}_\perp, \omega - \Omega)\zeta_{-\Omega,\Omega}^*. \tag{3}$$

As can be seen from Eq. (3), the cascaded-field generation requires $\hat{E}_s^{(m-1)}(\omega)$ as given by Eq. (2) to describe the higher-order MIR contributions [in the same way that Eq. (2) requires (3)], with $\hat{E}_s^{(1)}(\omega) \equiv \delta\hat{E}_s(\omega)$ being the vacuum NIR electric field. The factor $\zeta_{\pm\Lambda,\Omega} = \mp id\frac{L\Lambda}{2c_0 n}\text{sinc}[\frac{L\Omega}{2c_0}(n_\Omega - n_g)]\exp[i\frac{L\Omega}{2c_0}(n_\Omega - n_g)]$ determines phase matching. Here $n_g = c_0\partial k_\omega/\partial\omega$ is the group RI, taken at the central probe frequency. The total generated field in each of the frequency ranges is then $\Delta\hat{\mathbf{E}}'(\Lambda) = \sum_{m>1}\hat{\mathbf{E}}^{(m)}(\Lambda)$, and accordingly $\hat{\mathbf{E}}'(\omega) = \mathbf{E}_p(\omega) + \delta\hat{\mathbf{E}}(\omega) + \Delta\hat{\mathbf{E}}'(\omega)$ for the analyzed NIR.

After the NX, the detection part of the setup consists of an ellipsometer including two balanced photon counters that record the statistics of the photon numbers $\hat{\mathcal{N}}_s$ and $\hat{\mathcal{N}}_z$ for the s- and z-polarization components of the output NIR field [cf. Fig. 1(b)]. For the evaluation of the quantum signal $\hat{S} = \hat{\mathcal{N}}_s - \hat{\mathcal{N}}_z$, we may neglect quadratic or higher-order terms in $\delta\hat{E}$. $\delta\hat{E}_s(\Lambda)$ is given by Eq. (1) with transverse mode functions $g'_{l_p}(\mathbf{r}_\perp) \equiv \text{LG}_{l_p}(\mathbf{r}_\perp, 0; \Lambda)$. The total signal can be split into EO and base-SN contributions $\hat{S} = \hat{S}_{\text{EO}} + \hat{S}_{\text{SN}}$. In a perturbative approach, the contributions to the EO signal $\hat{S}_{\text{EO}} = \sum_{j=1}^{\infty}\hat{S}^{(j)}$ are given by

$$\hat{S}^{(j)} = i\sqrt{B}A^{(j+1)}\int_0^{\infty} d\Omega \sqrt{\frac{\Omega}{n_\Omega}}\big[\hat{a}_{s00}^{(j)}(\Omega)R(\Omega) - \text{H.c.}\big], \tag{4}$$

where $A^{(j+1)} = \int d^2r_\perp g_{00}^{j+1}(\mathbf{r}_\perp)g'_{00}(\mathbf{r}_\perp)$ and $\hat{a}_{s00}^{(j)}$ is the Bogoliubov-transformed (outgoing) annihilation operator, given by a series of nested convolutions of $\hat{a}_{s00}(\Lambda)$ with functions covering either MIR or NIR frequencies depending on the value of j [20,21]. In Eq. (4), $B = (d^2L^2N^2\omega_p^2\hbar)/(4\pi\epsilon_0 c_0^3 n^2)$ and $1/\omega_p = \beta/\kappa$ is the average inverse detected frequency, with $\beta = \int_0^{\infty}\frac{d\omega}{\omega}|\alpha_p(\omega)|^2$ and $\kappa = \int_0^{\infty} d\omega|\alpha_p(\omega)|^2$. We have introduced the expectation value of the photon number per probe pulse $N = \langle\hat{\mathcal{N}}_s + \hat{\mathcal{N}}_z\rangle = \frac{4\pi c_0 n\epsilon_0}{\hbar}\beta$ and the gating function $R(\Omega) = i\zeta_{\omega,\Omega}[f_+^*(\Omega) + f_-(\Omega)]/(d\frac{L\omega}{c_0 n})$ with $f_\pm(\Omega) = \int_0^{\infty} d\omega \, \alpha_p^*(\omega)\alpha_p(\omega \pm \Omega)/\kappa$ determining the bandwidth over which states can be measured. The base-SN contribution is given by

$$\hat{S}_{\text{SN}} \equiv \hat{S}^{(0)} = \sqrt{4\pi c_0 n\epsilon_0}\int_0^{\infty} d\omega\frac{\alpha_p^*(\omega)\hat{a}_{s00}(\omega) + \text{H.c.}}{\sqrt{\hbar\omega}}. \tag{5}$$

For a nondisplaced quantum state like the vacuum, $\langle\hat{S}^{(j)}\rangle = 0 \,\forall\, j \in \mathbb{N}$. When squared, however, the signals lead to finite expectation values associated with their variance $\langle\hat{S}^2\rangle = \langle[\sum_{j=0}^{\infty}\hat{S}^{(j)}]^2\rangle$. Through unfolding of the Bogoliubov transformations determining $\hat{a}_{s00}^{(j)}(\Omega)$, it is possible to see that, depending on j, the EO signals are functionals of either $\hat{a}_{s00}(\Omega)$ (for j odd) or $\hat{a}_{s00}(\omega)$ (for j even). Apart from $\langle[\hat{S}^{(j)}]^2\rangle$, this leads to cross-term contributions to the variance in the form $\langle\hat{S}^{(j)}\hat{S}^{(j+2)}\rangle$, $\langle\hat{S}^{(j)}\hat{S}^{(j+4)}\rangle$, and so on, as well as their conjugates. If one decomposes the

total signal into terms depending solely on $\hat{a}(\Omega)$ and $\hat{a}(\omega)$, $\sum_{\text{odd }j}\hat{S}^{(j)}$ and $\sum_{\text{even }j}\hat{S}^{(j)}$, these two contributions would be effectively related via a two-mode squeezing involving one (nonmonochromatic) mode from each frequency range, MIR and NIR [22]. For this reason, the noise registered in the NIR is larger than the base level determined by $\langle\hat{S}_{\text{SN}}^2\rangle = N$.

The main contribution of the electric-field fluctuations in the MIR vacuum [32] to the EO signal variance is $\langle(\hat{S}^{(1)})^2\rangle \propto N^2\int_0^{\infty} d\Omega \, \Omega (n/n_\Omega)|R(\Omega)|^2$, as shown in Appendix A and experimentally endorsed by Ref. [10] (see also [28]). This term represents the zero-point variance of the electric field $\langle\delta\hat{E}_s(\mathbf{r}_\perp, \Omega)\delta\hat{E}_s(\mathbf{r}'_\perp, \Omega')\rangle$, sampled over a frequency window determined by $R(\Omega)$ and over a transverse spatial profile determined by $g_{00}^2(\mathbf{r}_\perp)$.

Complementary to $\langle(\hat{S}^{(1)})^2\rangle$, there is the cross term between $\hat{S}^{(2)}[\hat{E}_s^{(3)}(\omega)]$ and $\hat{S}_{\text{SN}}[\delta\hat{E}_s(\omega)]$. This term has not been accounted for in Refs. [17,28,33,34], but its contribution vanishes when the measurements are carried out far from any resonances. Interestingly, both $\langle\hat{S}^{(2)}\hat{S}^{(0)} + \hat{S}^{(0)}\hat{S}^{(2)}\rangle$ and $\langle\hat{S}^{(1)}\hat{S}^{(1)}\rangle$ share contributions from the first- and second-order perturbations in the initial sampled state from a state-evolution perspective (cf. Appendix G). Some of them retain the MIR sector of the vacuum unchanged, while others correspond to populated MIR modes. Figure 1(c) sketches the annihilation (red) and creation (green) of photons by the Hamiltonian when acting on the vacuum (top, annihilating a probe photon to create an MIR and an NIR photon) and on its first-order perturbation (showing the action of the four different three-photon contributions in the Hamiltonian), with the second and third processes leading to no MIR photons in the perturbed state, while the last two lead to an increase in the number of MIR photons. These perturbations are the source of EO signals and are comprised of a continuum of states in superposition with the initial state. As long as their superposition coefficients are much smaller than the coefficient of the initial state, the first- and second-order perturbations of the initial state are the dominating BA and the measurement of the vacuum noise can be seen as effectively free of BA. As N increases, further BA-induced contributions with coefficients growing even faster with N, such as the ones contributing to $\langle[\hat{S}^{(2)}]^2\rangle$ and terms involving $\hat{S}^{(j>2)}$, become significant in the quantum superposition of states, with our perturbation approach breaking down as they start to dominate.

III. SINGLE-CHANNEL RESULTS

To evaluate the BA effect on the measurement results, we derive all contributions from Eqs. (2) and (3) to the EO signal variance up to fourth order. The cross term between the SN signal and $\hat{S}^{(4)}[\hat{E}^{(5)}(\omega)]$ vanishes within our approximations. The remaining $\hat{a}(\omega)$-dependent contribution, which also enhances the base SN, results from $\langle[\hat{S}^{(2)}]^2\rangle$ and scales as N^3. Concurrent to this contribution is the $\hat{a}(\Omega)$-dependent (cross) term $\langle\hat{S}^{(1)}\hat{S}^{(3)} + \hat{S}^{(3)}\hat{S}^{(1)}\rangle$, which scales as N^3 but has an opposite sign to $\langle[\hat{S}^{(2)}]^2\rangle$. Consequently, it leads to variance reduction.

Figure 2 illustrates the total root-mean-square (rms) signal per probe photon as a function of N. For comparison, we provide plots corresponding to the experimental parameters of Refs. [28] (set 1, a) and [17] (set 2, b). For the probe pulses
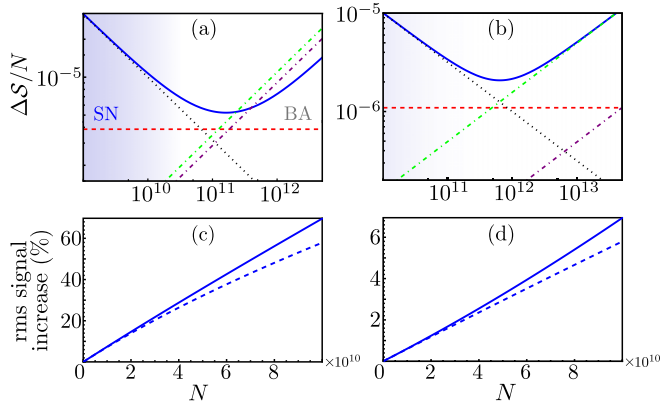
FIG. 2. (a), (b) Ratio $\Delta\mathcal{S}/N$ (with the rms signal $\Delta\mathcal{S} = \langle\hat{\mathcal{S}}^2\rangle^{1/2}$) in dependence of the number N of photons per probe pulse. The solid blue lines represent the total rms signal per photon, the dotted black lines represent the base-SN contribution, the dashed red lines show the main EO rms signal, and the green (purple) dotted-dashed lines account for $\langle[\hat{\mathcal{S}}_{EO}^{(2)}]^2\rangle$ $[\langle\hat{\mathcal{S}}_{EO}^{(1)}\hat{\mathcal{S}}_{EO}^{(3)} + \hat{\mathcal{S}}_{EO}^{(3)}\hat{\mathcal{S}}_{EO}^{(1)}\rangle]$. The background gradient illustrates the transition between the effectively BA-free, shot-noise dominated (SN), and the BA-dominated (BA) regimes. (c), (d) Increase of $(\Delta\mathcal{S} - \Delta\mathcal{S}_{SN})/\Delta\mathcal{S}_{SN}$ with N. The solid (dotted) blue lines contain up to fourth- (second-) order contributions. (a), (c) [(b), (d)] Correspond to parameter set 1 (set 2) (see main text).

we assume $\omega_p^{(set\ 1)}/(2\pi) = 247$ THz and $\omega_p^{(set\ 2)}/(2\pi) = 375$ THz, and spectral bandwidths of $\Delta\omega_p^{(set\ 1)}/(2\pi) = 150$ THz and $\Delta\omega_p^{(set\ 2)}/(2\pi) = 2.77$ THz with rectangular spectral amplitude distributions and flat phase. We consider beam waist radii of $w_0^{(set\ 1)} = 3$ µm and $w_0^{(set\ 2)} = 125$ µm. For the NX we use $L^{(set\ 1)} = 7$ µm and $L^{(set\ 2)} = 3$ mm, $r_{41} = 3.9$ pm/V, $n^{(set\ 1)} = 2.76$, $n^{(set\ 2)} = 2.85$, $n_g^{(set\ 1)} = 2.9$, $n_g^{(set\ 2)} = 3.18$ and n_Ω varying slightly within the relevant THz frequency range (cf. Appendix E). We do not include contributions from four-wave mixing since they only affect the probe (for more details, see Appendix F). Figure 2 reveals a considerable deviation from the result determined solely by the SN and the main EO contribution [28] when photon numbers are larger than $\sim 10^{11}$. Minima in the rms signal per probe photon occur at $N = 1.6 \times 10^{11}$ for set 1 [Fig. 2(a)] and $N = 6.4 \times 10^{11}$ for set 2 [Fig. 2(b)], i.e., roughly when $\langle[\hat{\mathcal{S}}^{(1)}]^2\rangle \sim \langle[\hat{\mathcal{S}}_{SN}]^2\rangle$. Contrary to naive expectations that $\langle(\hat{\mathcal{S}}^{(1)})^2\rangle$ would generally dominate the total rms signal for large N, our results show that increasing the probe intensity beyond a certain value has a rather detrimental effect since both the base SN and main EO signal variance are rapidly overtaken by the cascaded effects. Therefore, a reliable minimally disturbing quantum-state sampling may be achieved only for N considerably smaller than its value at the minima of the solid blue curves in Figs. 2(a) and 2(b). Figures 2(c) and 2(d) show the (normalized) detected rms signal on top of the base SN contribution. Departure from zero allows for a clear visualization of the EO contributions, with the onset of the fourth-order terms resulting in a divergence between the solid and the dashed blue lines in each figure. The threshold for the regime dominated by BA is analyzed in Appendix B.
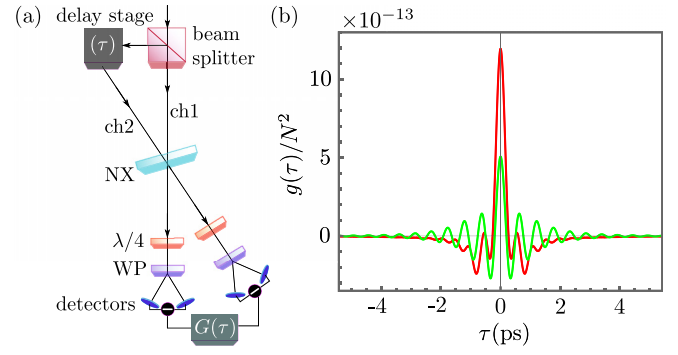

FIG. 3. (a) EO measurement with two channels (ch1 and ch2), with $\lambda/4$, WP, and $G(\tau)$ representing the quarter-wave plate, the Wollaston prism, and the correlation register. (b) Total second-(red) and fourth-order (green) contributions to $g(\tau)$ for $N = 10^{11}$, representing correlations in the two-channel measurements.

IV. TWO-CHANNEL MODEL

For a two-channel setup [Fig. 3(a)], the probe beam undergoes a beam-splitting operation before any of the processes discussed before [see Fig. 1(b)]. The two probe pulses released from a 50:50 beam splitter not only carry different phases (reflected and transmitted beams differ in phase by $\pi/2$), but also commuting annihilation and creation operators due to the admixture of uncorrelated vacuum noise (cf. Appendix C). Once the first probe pulse meets the NX, its interactions with the MIR vacuum will generate the BA contributions as discussed above. The second probe pulse reaches the NX with a time delay τ and interacts not only with that MIR vacuum, but also with the BA contributions generated by the passage of the first probe. It will also generate its own BA contributions that can interact with the first probe. Each channel output undergoes its own ellipsometry detection. The signals from the two channels, $\hat{\mathcal{S}}_{ch1}$ and $\hat{\mathcal{S}}_{ch2}$, are then multiplied before readout, rendering a delay-dependent signal variance with the properties of a correlation function: $G(\tau) = \frac{1}{2C}\langle 0|\{\hat{\mathcal{S}}_{ch2}(\tau), \hat{\mathcal{S}}_{ch1}(\tau)\}|0\rangle = \frac{1}{C}g(\tau)$ with $C = (n^3 L\omega_p r_{41}N/c_0)^2$ [17]. The subscripts ch1 and ch2 shall describe quantities related to the channels 1 and 2, respectively.

We consider a setup in which the directions of the central wave vectors of the beams in the two channels deviate only slightly from each other (i.e., $\mathbf{k}_{ch1} \cdot \mathbf{k}_{ch2} \approx k_{ch1}k_{ch2}$). This allows for consideration of effectively coplanar beam waists in the NX, as well as nearly collinear phase matching for the wave-mixing processes. Therefore, the treatment of fields in terms of the paraxial decomposition remains well justified. To avoid considerable deviations of output wave vectors from either $\mathbf{k}_{ch1}$ or $\mathbf{k}_{ch2}$, only the second set of parameters will be considered. Due to the limited beam waist, mixing between modes from different channels during the ellipsometry step is avoided. For the quantum fluctuations of the probe pulses $[\hat{a}_{ch1}(\omega), \hat{a}_{ch2}^\dagger(\omega')] = 0$, leading to $\langle\{\hat{\mathcal{S}}_{ch1}^{(0)}, \hat{\mathcal{S}}_{ch2}^{(0)}\}\rangle = 0$ [cf. (5)]. Consequently, while SN still affects the measurements, the two-channel equivalent of the base SN does not contribute to $g(\tau)$. In general, the (time-dependent) signal operators are given by equations similar to Eq. (4). The cascaded contributions (2) and (3) (for $m \geqslant 2$) are now composed of convo-

lutions with either $E_{p,ch2}(\omega)e^{-i(\omega\tau+\pi/2)}$ or $E_{p,ch1}(\omega)$, splitting each single-channel contribution $\hat{E}_s^{(m)}$ into 2^{m-1} terms. Ellipsometry conducted with either of these fields then leads to $\hat{\mathcal{S}}_{ch2}^{(j)}$ or $\hat{\mathcal{S}}_{ch1}^{(j)}$, respectively (cf. Appendix D). Since oscillations in τ with NIR frequencies can neither be resolved nor are of major interest in such an experiment, only contributions to $G(\tau)$ oscillating at MIR frequencies will be considered.

V. TWO-CHANNEL RESULTS

Figure 3(b) shows $g(\tau)$ with all terms up to fourth order. The main contribution, which depends on $\hat{E}_{ch1}^{(2)}(\tau)\hat{E}_{ch2}^{(2)}(\tau)$, is proportional to $N^2 \int_0^\infty d\Omega\,\Omega\,(n/n_\Omega)|R(\Omega)|^2 \cos(\Omega\tau)$. This behavior is also seen in the measured data in Ref. [17] up to differences in spectral shape chosen for the probe. Contributions from higher-order terms are minor up to $N \sim 10^{11}$, where they become comparable to the second-order contributions. For $N \sim 10^8$, as in experiments [11,12,17], higher-order contributions to $G(\tau)$ are negligible.

The characteristic timescale of $G(\tau)$ is similar to that of the two probe pulses since the multiplied signal is nonzero only when they share interactions with the same propagating MIR modes [35] . The oscillations of $G(\tau)$ in Fig. 3(b) happen with a timescale approximately inverse to the average probed MIR (angular) frequency and reflect the interference between modes from different channels [36,37]. From a state-evolution perspective, $G(\tau)$ includes interchannel probe-probe correlations mediated by MIR states, populated or not (see Appendix G).

VI. CONCLUSIONS

Our results show that in single-channel quantum EO measurements of the electromagnetic vacuum there is a suitable setup-dependent range of probe intensities to minimize the contributions from (measurement-)generated MIR photons to the signal. For small (large) probe intensities, the results are inevitably contaminated by excessive SN (BA). The photon numbers where $\langle[\hat{\mathcal{S}}^{(1)}]^2\rangle \sim \langle[\hat{\mathcal{S}}_{SN}]^2\rangle$ represent upper limits to the experimentally admissible probe intensities to avoid BA predominance. The BA to the MIR states is inherent to the EO measurement but the detected MIR signal variance can be considered effectively BA free (weak measurement) for small perturbations of the MIR states. Creation of MIR photons considerably changes the picture of EO sampling as a potential quantum nondemolition measurement since notwithstanding its indirect character (with the MIR as sample and NIR as ancilla), a postselection scheme is needed to filter components of the sample without generated photons. Furthermore, the base-SN contribution does not show up in the averaged correlations measured with two channels, while enhanced SN contributions appear for probe intensities orders of magnitude above the experimentally used. Future works might explore postselection to achieve further BA evasion.

APPENDIX A: HIGHER-ORDER CONTRIBUTIONS TO THE SIGNAL VARIANCE

In this Appendix, we provide the expressions for the higher-order contributions (in terms of powers of the susceptibility or of the probe photon number) to the signal variance. All equations have been derived with the aid of Eqs. (2)–(4), which give nested convolutions when applied alternatively m times. The signal operator is given by the difference between the number operators $\hat{\mathcal{N}}_{s/z}^{(m)} = 4\pi c_0 n\epsilon_0 \int \frac{d\omega}{\hbar\omega} \int d^2 r_\perp \hat{E}_{s/z}''^{(m)\dagger}(\mathbf{r}_\perp, \omega)\hat{E}_{s/z}''^{(m)}(\mathbf{r}_\perp, \omega)$ for the z and s polarizations, with the double primes denoting the post-wave-plate electric-field operators. When the expectation values of quadratic combinations of signal operators with respect to the vacuum state are taken, the creation operator from one signal and the annihilation operator from the other signal will provide the needed delta function [i.e., $\langle \hat{a}_{s00}(\Lambda)\hat{a}_{s00}^\dagger(\Lambda')\rangle = \delta(\Lambda - \Lambda')$] to tie the convolutions in the two signal operators together. Integrals at the ends of the nested convolutions give terms of the form (A4), while the term (A5) appears in the center of larger nested convolutions, as shown below.

Apart from the main contribution to the signal variance given by

$$\langle(\hat{\mathcal{S}}^{(1)})^2\rangle = N^2 \left(n^3 \frac{L\omega_p}{c_0}r_{41}\right)^2 \frac{\hbar \int_0^\infty d\Omega\,\Omega\,(n/n_\Omega)|R(\Omega)|^2}{4\pi^2\epsilon_0 c_0 n w_0^2},$$
(A1)

there is another contribution of second order in r_{41} arising from the cross term between the SN signal and the signal arising from the measurement of the field $\hat{E}_s^{(3)}(\omega)$ (i.e., the field generated when the nonlinear mixing with the probe takes the NIR vacuum field to the MIR and this new generated MIR field mixes then once again with the probe to give a NIR field). The respective contribution to the signal variance is given by

$$\langle\{\hat{\mathcal{S}}^{(2)}, \hat{\mathcal{S}}_{SN}\}\rangle = -\frac{2C_1}{\sqrt{3}} \int_{-\infty}^\infty d\Omega\,\Omega \frac{2c_0 n^2}{n_\Omega dL\omega}[i\zeta_{\omega,\Omega}f_-(\Omega)R^*(\Omega)],$$
(A2)

where

$$C_j = N^{j+1}\left(n^3 \frac{L\omega_p}{c_0}r_{41}\right)^{2j}\left(\frac{\hbar}{4\pi^2\epsilon_0 c_0 n w_0^2}\right)^j$$
(A3)

and $j \in \mathbb{N}$. The spatial integral for $\hat{\mathcal{S}}^{(2)}$ (with $w_0' = w_0/\sqrt{3}$) gives $A^{(3)} = (2/\sqrt{3\pi^2})/w_0^2$. Note that the variable ω^{-1} in Eq. (A2) gets canceled by the ω in $\zeta_{\omega,\Omega}$, so that the result does not depend on it. For our specific choice of the probe profile, $f_-(\Omega) = F(\Omega) \equiv \frac{1}{2}[f_+^*(\Omega) + f_-(\Omega)]$ within the range of MIR frequencies selected by the phase matching, making the

integrand an even function of Ω. Hence, the right-hand side of Eq. (A2) vanishes.

Before delving into the fourth-order contributions to the signal variance, it is worth introducing some building-block functions that will be used through the remainder of the Appendix:

$$R_i^{(\pm)}(\Omega, X, \tau) = \frac{1}{2} \operatorname{sinc}\left[\frac{L\Omega}{2c_0}(n_\Omega - n_g)\right] e^{\frac{iL\Omega}{2c_0}(n_\Omega - n_g)} \frac{\int_{-\infty}^{\infty} d\omega\, \alpha_p^*(\omega)\alpha_p(\omega - \Omega)K_i^{(\pm)}(\omega, X, \tau)}{\int_0^{\infty} d\omega\, |\alpha_p(\omega)|^2},$$ (A4)

$$W_i^{(\pm)}(\Omega, \Omega', X, \tau) = \frac{\int_{-\infty}^{\infty} d\omega\, \omega \alpha_p^*(\omega - \Omega)K_i^{(\pm)}(\omega, X, \tau)\alpha_p(\omega - \Omega')}{\int_0^{\infty} d\omega\, |\alpha_p(\omega)|^2},$$ (A5)

$$G_{ij}^{(\pm,\pm')}(\Omega, \Omega', X, Y, \tau) = \left(d\frac{L\omega_p^{3/2}}{2c_0 n}\right)^{-2} \zeta_{\omega_p,\Omega}^* \zeta_{\omega_p,\Omega'} R_i^{(\pm)}(\Omega, X, \tau) W_j^{(\pm')}(\Omega, \Omega', Y, \tau).$$ (A6)

The functions $K_i^{(\pm)}$ can have different shapes depending on the choice of the index i, namely, $K_0^{(\pm)}(\omega, X, \tau) = \theta(\pm\omega)$, $K_1^{(\pm)}(\omega, X, \tau) = \cos[\tau(\omega + X)]\theta(\pm\omega)$, and $K_2^{(\pm)}(\omega, X, \tau) = \sin[\tau(\omega + X)]\theta(\pm\omega)$. Here $\theta(x)$ denotes the Heaviside step function. In the trivial $i = 0$ case, we have

$$\sum_{s=\pm} R_0^{(\pm)}(\Omega) = \operatorname{sinc}\left[\frac{L\Omega}{2c_0}(n_\Omega - n_g)\right] e^{\frac{iL\Omega}{2c_0}(n_\Omega - n_g)}$$
$$\times (1 - |\Omega|/\Delta\omega)\theta(1 - |\Omega|/\Delta\omega) = R(\Omega).$$ (A7)

There are three fourth-order contributions to the signal variance. One of them is just the square of the signal associated with $\hat{E}_s^{(3)}(\omega)$ field mentioned above (i.e., shot-noise enhancement). The corresponding expression is given by

$$\langle (\hat{\mathcal{S}}^{(2)})^2 \rangle = \frac{C_2}{3} \sum_{t=\pm} \int_{-\infty}^{\infty} d\Omega \int_{-\infty}^{\infty} d\Omega'$$
$$\times (\Omega\Omega') R^*(\Omega') G_{00}^{(t,+)}(\Omega, \Omega', 0, 0, 0).$$ (A8)

The second term of same perturbative order results from the mixing between the main signal $\hat{\mathcal{S}}^{(1)}[\delta\hat{E}_s(\Omega)]$ and the signal $\hat{\mathcal{S}}^{(3)}[\hat{E}_s^{(3)}(\Omega)]$, giving

$$\langle\{\hat{\mathcal{S}}^{(3)}, \hat{\mathcal{S}}^{(1)}\}\rangle = \frac{-C_2}{\sqrt{2}} \sum_{t,s=\pm} \int_{-\infty}^{\infty} d\Omega \int_0^{\infty} d\Omega'$$
$$\times (\Omega\Omega') R^*(\Omega') G_{00}^{(t,s)}(\Omega, \Omega', 0, 0, 0) \frac{n}{n_{\Omega'}}.$$ (A9)

Here, $A^{(4)} = \sqrt{2/\pi^3}/w_0^3$ for $\hat{\mathcal{S}}^{(3)}$ with $w_0' = w_0/2$. The last contribution comes from the cross term between the SN and the signal $\hat{\mathcal{S}}^{(4)}[\hat{E}_s^{(5)}(\omega)]$ [with $A^{(5)} = 4/(\sqrt{5}\pi^2 w_0^2)$ for $w' = w_0/\sqrt{5}$]. This term gives zero variance contribution for our choice of the probe profile, similarly to Eq. (A2) [because $\sum_t W_0^{(t)}(\Omega, \Omega') = -\sum_t W_0^{(t)}(-\Omega, -\Omega')$]:

$$\langle\{\hat{\mathcal{S}}_{EO}^{(4)}, \hat{\mathcal{S}}_{SN}\}\rangle = \frac{C_2}{\sqrt{5}} \sum_{t,s=\pm} \int_{-\infty}^{\infty} d\Omega \int_{-\infty}^{\infty} d\Omega'(\Omega\Omega')$$
$$\times R_0^{(+)*}(\Omega', 0, 0) G_{00}^{(t,s)}(\Omega, \Omega', 0, 0, 0).$$ (A10)

APPENDIX B: INFLUENCE OF THE BEAM WAIST AND ONSET OF CASCADED-CONTRIBUTION SIGNALS

The threshold for the regime dominated by BA is illustrated in Fig. 4 in dependence of the beam waist radius w_0. In Figs. 4(a) and 4(b), one can see how the minimum of the total rms signal per photon (at the minimizing N value, $N_{\min}$) depends on w_0 [normalized by $L^{(\text{set }1)}$ and $L^{(\text{set }2)}$, respectively]. For comparison, we also show the dependencies of the SN and main ($j = 1$) rms signals per photon on w_0 at $N = N_{\min}$. One can see that $\Delta\mathcal{S}/N(N_{\min}, L/w_0)$ increases linearly with L/w_0 and its slope is larger than the ones for both the SN and the main EO contributions, which also grow linearly. One can therefore expect that increasing the length-to-waist ratio makes the detection of the vacuum signal more difficult.

APPENDIX C: PRODUCT SIGNAL WITH TWO PROBE BEAMS

In this Appendix we discuss in more details the subtleties of the theoretical description in case of the measurement scheme implemented in Ref. [17]. One of the key features of this experiment is the use of a beam splitter to convert a single probe pulse into two pulses of equal durations. The beam splitter mixes the coherent probe of classical amplitude α_p and its quantum vacuum contribution (described by operators $\hat{a}$) with the vacuum noise (represented by operators $\hat{a}_{\text{free}}$) accessing the classically free port of the device. The resulting transformation of the incoming probe field is given by

$$\begin{aligned} \hat{a}_1^{(\text{out})}(\omega) &= T(\omega)\hat{a}_1^{(\text{in})}(\omega) + R'(\omega)\hat{a}_2^{(\text{in})}(\omega) \\ &= T(\omega)\alpha_p(\omega) + [T(\omega)\hat{a}(\omega) + R'(\omega)\hat{a}_{\text{free}}(\omega)] \\ &= T(\omega)\alpha_p(\omega) + \hat{a}_{p,\text{ch}1}(\omega), \\ \hat{a}_2^{(\text{out})}(\omega) &= R(\omega)\hat{a}_1^{(\text{in})}(\omega) + T'(\omega)\hat{a}_2^{(\text{in})}(\omega) \\ &= R(\omega)\alpha_p(\omega) + [R(\omega)\hat{a}(\omega) + T'(\omega)\hat{a}_{\text{free}}(\omega)] \\ &= R(\omega)\alpha_p(\omega) + \hat{a}_{p,\text{ch}2}(\omega). \end{aligned}$$ (C1)

It is worth mentioning that this transformation applies for all frequencies, including the MIR frequency range, in which $\alpha_p(\omega) = 0$. The new annihilation operators $\hat{a}_{p,\text{ch}1}$ and $\hat{a}_{p,\text{ch}2}$
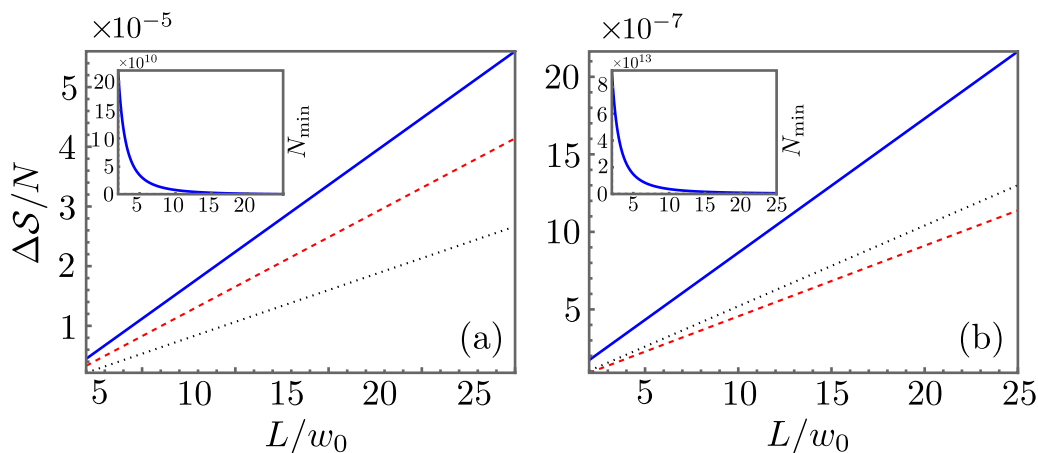
FIG. 4. Minimum of $\Delta\mathcal{S}/N$ as a function of w_0. The solid blue line shows the total $\Delta\mathcal{S}/N$ value. The dotted black (dashed red) lines represent the SN (main EO) contributions. The insets show how the probe photon number that minimizes $\Delta\mathcal{S}/N$, $N_{\min}$, varies as a function of w_0 (also normalized as L/w_0). (a), (b) Correspond to parameter sets 1 and 2, respectively, apart from the value of w_0.

are associated with the two channels employed in the experiment. One interesting feature of the output operators is their commutativity: $[\hat{a}_{p,ch1}, \hat{a}_{p,ch2}^\dagger] = TR^* + R'T'^* = 0$ under the assumption of a dissipationless beam splitter. As a result, the product of two signals, each of which is a functional of beam-splitter creation and annihilation output operators originating from a different channel, has vanishing expectation value. A less pronounced but also important feature is the phase introduced by the beam splitter on the reflected components of the fields. For the sake of agreement with the particular experimental realization, we shall consider an ideal 50:50 beam splitter without dispersion, with $T = T' = 1/\sqrt{2}$ and $R = R' = i/\sqrt{2}$.

To account for the relative delay between modes in different channels, we consider the channel-two modes to be time shifted by a delay τ relative to the channel-one modes. This effectively introduces a factor $e^{-i\Lambda\tau}$ on the positive-frequency components of the channel-two fields when working in the frequency domain. Assuming that the fields from both channels meet at the NX in a quasiparallel configuration (i.e., the angle between them is $\lesssim 5°$), so that cross-section and propagation-length mismatch can be neglected at the focus of the beams and the frequency decomposition of fields can substitute the wave-vector one, wave mixing will involve contributions from both channels. Hence, the τ-dependent phase (with a suitable frequency argument) can appear at any (if not several) steps when applying Eqs. (2) and (3). There are, however, constraints on the possibilities of combination of phase factors in the convolutions of field operators with (time-shifted) probe pulses, based on the actual spatial distribution of output wave vectors. Since $\mathbf{k}_\Omega$ effectively does not affect the direction of $\mathbf{k}_{\omega,ch1/2}$, so that $\mathbf{k}_{\omega,ch1/2} \pm \mathbf{k}_\Omega \approx \mathbf{k}_{\omega\pm\Omega,ch1/2}$ for either channel, combinations of fields from different channels should be such that the sum of wave vectors involved in the nested convolutions aligns with the input wave vector of one of the channels: $\sum_i \mathbf{k}_i \approx \mathbf{k}_{ch1/2}$. This leads to a set of effective selection rules:

(i) Convolution of two field contributions from the same channel [e.g., by consecutive application of Eqs. (2) and (3) with the same probe] does not contribute to the final wave vector since such a same-channel convolution involves two wave vectors that are opposite to each other.

(ii) For fields that are functionals of the NIR annihilation and creation operators, contributions to the expectation value of a product of two signal operators will not vanish only when both multiplied signals depend on operators from the same channel: the output in one of the channels should carry NIR annihilation and creation operators from the other channel or, equivalently, the sum of wave vectors corresponding to a given $\hat{E}_{s,ch2/1}^{(m)}(\omega)$ should take the input vector $\mathbf{k}_{ch1/2}$ of $\delta\hat{E}_{s,ch1/2}(\omega)$ to the output $\mathbf{k}_{ch2/1}$.

(iii) Only odd total numbers of τ-dependent phase factors distributed between the nested convolutions in both $\hat{E}_{s,ch1}^{(m)}(\omega)$ and $\hat{E}_{s,ch2}^{(m')}(\omega)$ lead to cross signals with oscillations at MIR frequencies.

The ellipsometry step takes place independently for each channel, with channel-one fields being superposed with $E_{p,ch1}$ and channel-two fields with $E_{p,ch2}$, respectively. For this reason, the base SN signals in each channel commute with each other [these signals in channels one and two are proportional to integrals over $\hat{a}_{p,ch1}(\omega)$ and $\hat{a}_{p,ch2}(\omega)$, respectively, as well as their corresponding conjugates]. This commutation relation is what allows the measurement of the product of signals from different channels to have its base SN contribution reduced to negligible values over a large enough averaging sample, at least as long as SN enhancement does not become appreciable. Upon multiplication of the signals from the two channels, each signal-variance component treated in the previous section will now give rise to a plethora of time-dependent components, many of which oscillate with frequencies in the bandwidth of the probe. The latter components will not be considered in this work since with their high-frequency oscillations they effectively just average out to zero in the discussed experiment. With the purpose of comparison, we shall consider the beam-splitter output probes to have the same intensity as the probes used in the single-channel calculations.

APPENDIX D: CORRELATION FUNCTIONS

Upon application of the selection rules introduced in the Appendix C it is possible to reduce the total of 56 contributions to the correlation function (up to fourth order) to just a few. At second order, only two out of the eight possible outcomes fulfill the selection rules. We start by the description of the mainly contributing second-order term, the squared MIR vacuum signal of the form

$$\frac{1}{2}\langle \hat{\mathcal{S}}_{\text{ch1}}^{(1)}\hat{\mathcal{S}}_{\text{ch2}}^{(1)} + \hat{\mathcal{S}}_{\text{ch2}}^{(1)}\hat{\mathcal{S}}_{\text{ch1}}^{(1)}\rangle(\tau)$$
$$= C_1 \int_{-\infty}^{\infty} d\Omega\, \Omega\, \frac{n}{n_\Omega} |R(\Omega)|^2 \cos(\Omega\tau). \quad \text{(D1)}$$

Its time dependence comes from the delay in one of the channels, introducing an $e^{-i(\omega-\Omega)\tau}$ phase factor on the (channel-two) field that mixes with the MIR vacuum in Eq. (2) and an $e^{-i\omega\tau}$ on the probe that takes part in the (channel-two) ellipsometry, resulting in the overall $\Omega\tau$ dependence. The other contribution of second order reads

$$\frac{1}{2}\langle\{\hat{\mathcal{S}}_{\text{ch1}}^{(2)},\hat{\mathcal{S}}_{\text{ch2}}^{(0)}\} + \{\hat{\mathcal{S}}_{\text{ch1}}^{(0)},\hat{\mathcal{S}}_{\text{ch2}}^{(2)}\}\rangle(\tau) = \frac{-2C_1}{\sqrt{3}}\int_{-\infty}^{\infty}d\Omega\,\Omega\,(n/n_\Omega)$$
$$\times\left[i\zeta_{\omega,\Omega}f_-(\Omega)R^*(\Omega)\cos(\Omega\tau)\bigg/\left(d\frac{l\omega}{2c_0n}\right)\right]. \quad \text{(D2)}$$

This lowest-order cross-talk contribution results when the NIR electric-field fluctuations in one channel are down-converted to the MIR and then up-converted to the NIR at another channel. Under our approximations, this contribution vanishes.

On top of the cross-signal contributions (D1) and (D2), there are still contributions of higher perturbative orders. The next-order terms depend on N^3, and eventually overcome the N^2 terms as the probe-pulse intensity is increased. These N^3-dependent terms are similar in nature to the ones derived for the single-channel case, but differ in the many ways in which the probe pulses from the two channels can combine with the quantum components of the electromagnetic field. We shall therefore present them in the same order as we did in Appendix A.

The fourth-order contribution related to the $E_s^{(3)}(\omega)$ field can be split into three parts: $\frac{1}{2}\langle\hat{\mathcal{S}}_{\text{ch1}}^{(2)}\hat{\mathcal{S}}_{\text{ch2}}^{(2)} + \hat{\mathcal{S}}_{\text{ch2}}^{(2)}\hat{\mathcal{S}}_{\text{ch1}}^{(2)}\rangle(\tau) = V_{\{2,2\}}^{(a)}(\tau) + V_{\{2,2\}}^{(b)}(\tau) + V_{\{2,2\}}^{(c)}(\tau)$. Here, $V_{\{2,2\}}^{(a)}$ results from two equivalent processes: one in which the output of wave vector $\mathbf{k}_{\text{ch2}} - \mathbf{k}_{\text{ch2}}' + \mathbf{k}_{\text{ch2}}''$ is multiplied with the output corresponding to $\mathbf{k}_{\text{ch2}} - \mathbf{k}_{\text{ch2}}' + \mathbf{k}_{\text{ch1}}''$ and another in which the ch1 and ch2 subscripts are swapped.[1] $V_{\{2,2\}}^{(b)}$ originates from the product of field contributions with wave vectors $\mathbf{k}_{\text{ch1}} - \mathbf{k}_{\text{ch2}}' + \mathbf{k}_{\text{ch2}}''$ and $\mathbf{k}_{\text{ch1}} - \mathbf{k}_{\text{ch1}}' + \mathbf{k}_{\text{ch2}}''$, while $V_{\{2,2\}}^{(c)}$ results from the product of

contributions with wave vectors $\mathbf{k}_{\text{ch2}} - \mathbf{k}_{\text{ch2}}' + \mathbf{k}_{\text{ch1}}''$ and $\mathbf{k}_{\text{ch2}} - \mathbf{k}_{\text{ch1}}' + \mathbf{k}_{\text{ch1}}''$. Explicitly we find the following expressions:

$$V_{\{2,2\}}^{(a)}(\tau) = \frac{C_2}{3}\sum_{t,s=\pm}\int_{-\infty}^{\infty}d\Omega\int_{-\infty}^{\infty}d\Omega'(\Omega\Omega')R_0^{(s)*}(\Omega',0,0)$$
$$\times G_{00}^{(t,+)}(\Omega,\Omega',0,0,0)[\cos(\Omega\tau) + \cos(\Omega'\tau)], \quad \text{(D3)}$$

$$V_{\{2,2\}}^{(b)}(\tau) = \frac{C_2}{3}\sum_{s=\pm}\sum_{i=1,2}\int_{-\infty}^{\infty}d\Omega\int_{-\infty}^{\infty}d\Omega'(\Omega\Omega')R_0^{(s)*}$$
$$\times(\Omega',0,0)G_{ii}^{(+,+)}(\Omega,\Omega',\Omega',0,\tau), \quad \text{(D4)}$$

and

$$V_{\{2,2\}}^{(c)}(\tau) = \frac{C_2}{3}\sum_{s=\pm}\sum_{i=1,2}\int_{-\infty}^{\infty}d\Omega\int_{-\infty}^{\infty}d\Omega'(\Omega\Omega')R_i^{(+)*}$$
$$\times(\Omega',\Omega,\tau)G_{0i}^{(s,+)}(\Omega,\Omega',0,0,\tau). \quad \text{(D5)}$$

The behavior of each of the above contributions in dependence on the time delay τ is illustrated in Fig. 5.

The mixing between the main signal $\hat{\mathcal{S}}^{(1)}[\delta\hat{E}_s(\Omega)]$ and $\hat{\mathcal{S}}^{(3)}[\hat{E}_s^{(3)}(\Omega)]$ in the considered two-channel setup gives $\frac{1}{2}\langle\hat{\mathcal{S}}_{\text{ch1}}^{(3)}\hat{\mathcal{S}}_{\text{ch2}}^{(1)} + \hat{\mathcal{S}}_{\text{ch1}}^{(1)}\hat{\mathcal{S}}_{\text{ch2}}^{(3)} + \hat{\mathcal{S}}_{\text{ch2}}^{(3)}\hat{\mathcal{S}}_{\text{ch1}}^{(1)} + \hat{\mathcal{S}}_{\text{ch2}}^{(1)}\hat{\mathcal{S}}_{\text{ch1}}^{(3)}\rangle(\tau) = V_{\{1,3\}}^{(a)}(\tau) + V_{\{1,3\}}^{(b)}(\tau)$. Here, $V_{\{1,3\}}^{(a)}$ results from four equivalent processes: one in which the output of wave vector $\mathbf{k}_\Omega + \mathbf{k}_{\text{ch1}}' - \mathbf{k}_{\text{ch1}}'' + \mathbf{k}_{\text{ch1}}'''$ is multiplied with the output of vector $\mathbf{k}_\Omega + \mathbf{k}_{\text{ch2}}'$, another in which the output of wave vector $\mathbf{k}_\Omega + \mathbf{k}_{\text{ch2}}' - \mathbf{k}_{\text{ch2}}'' + \mathbf{k}_{\text{ch1}}'''$ is multiplied with the output with $\mathbf{k}_\Omega + \mathbf{k}_{\text{ch2}}'$, and the other two processes corresponding to swapped indices ch1 and ch2. $V_{\{1,3\}}^{(b)}$ originates from the product of field contributions with wave vectors $\mathbf{k}_\Omega + \mathbf{k}_{\text{ch1}}' - \mathbf{k}_{\text{ch2}}'' + \mathbf{k}_{\text{ch2}}'''$ and $\mathbf{k}_\Omega + \mathbf{k}_{\text{ch2}}'$ and the corresponding index-swapped counterpart. Explicitly we have

$$V_{\{1,3\}}^{(a)}(\tau) = \frac{-C_2}{\sqrt{2}}\sum_{t,s,u=\pm}\int_{-\infty}^{\infty}d\Omega\int_0^{\infty}d\Omega'(\Omega\Omega')R_0^{(u)*}(\Omega',0,0)$$
$$\times G_{00}^{(t,s)}(\Omega,\Omega',0,0,0)[\cos(\Omega\tau) + \cos(\Omega'\tau)]\frac{n}{n_{\Omega'}} \quad \text{(D6)}$$

and

$$V_{\{1,3\}}^{(b)}(\tau) = \frac{-C_2}{\sqrt{2}}\sum_{t,s=\pm}\sum_{i=1,2}\int_{-\infty}^{\infty}d\Omega\int_0^{\infty}d\Omega'(\Omega\Omega')\frac{n}{n_{\Omega'}}$$
$$\times R_0^{(s)*}(\Omega',0,0)G_{ii}^{(t,t)}(\Omega,\Omega',\Omega',0,\tau). \quad \text{(D7)}$$

The behaviors of $V_{\{1,3\}}^{(a)}(\tau)$ and $V_{\{1,3\}}^{(b)}(\tau)$ can be seen in Fig. 6.

The last fourth-order contribution, from the cross term between the base-SN signal and the signal $\hat{\mathcal{S}}^{(4)}[\hat{E}^{(5)}(\omega)]$ has the form $\frac{1}{2}\langle\hat{\mathcal{S}}_{\text{ch1}}^{(4)}\hat{\mathcal{S}}_{\text{ch2}}^{(0)} + \hat{\mathcal{S}}_{\text{ch1}}^{(0)}\hat{\mathcal{S}}_{\text{ch2}}^{(4)} + \hat{\mathcal{S}}_{\text{ch2}}^{(4)}\hat{\mathcal{S}}_{\text{ch1}}^{(0)} + \hat{\mathcal{S}}_{\text{ch2}}^{(0)}\hat{\mathcal{S}}_{\text{ch1}}^{(4)}\rangle(\tau) = V_{\{0,4\}}^{(a)}(\tau) + V_{\{0,4\}}^{(b)}(\tau) + V_{\{0,4\}}^{(c)}(\tau)$. As in the previous case, $V_{\{0,4\}}^{(a)}$ results from four equivalent processes: one in which the output of wave vector $\mathbf{k}_{\text{ch2}} - \mathbf{k}_{\text{ch2}}' + \mathbf{k}_{\text{ch2}}'' - \mathbf{k}_{\text{ch2}}''' + \mathbf{k}_{\text{ch1}}''''$ is multiplied with the SN output of vector $\mathbf{k}_{\text{ch2}}$, another in which the $\mathbf{k}_{\text{ch2}} - \mathbf{k}_{\text{ch2}}' + \mathbf{k}_{\text{ch1}}'' - \mathbf{k}_{\text{ch1}}''' + \mathbf{k}_{\text{ch1}}''''$ contribution combines with the same SN output, and the processes with ch1 and ch2 labels swapped. $V_{\{0,4\}}^{(b)}$ originates from the product of field contributions with wave vectors $\mathbf{k}_{\text{ch2}} - \mathbf{k}_{\text{ch2}}' + \mathbf{k}_{\text{ch1}}'' - \mathbf{k}_{\text{ch2}}''' + \mathbf{k}_{\text{ch2}}''''$ and $\mathbf{k}_{\text{ch2}}$, while $V_{\{0,4\}}^{(c)}$ results from the product of contributions

---

[1]In the schematic wave-vector description $\mathbf{k}_{\text{ch2}} - \mathbf{k}_{\text{ch2}}' + \mathbf{k}_{\text{ch1}}''$, the unprimed vector $\mathbf{k}_{\text{ch2}}$ represents the wave vector of the NIR operator $\delta\hat{E}_{\text{ch2}}(\omega)$, while the primed and doubly primed vectors stand for the wave vectors of the probe pulses participating in the first and second convolutions, respectively, that generate the output field contribution.
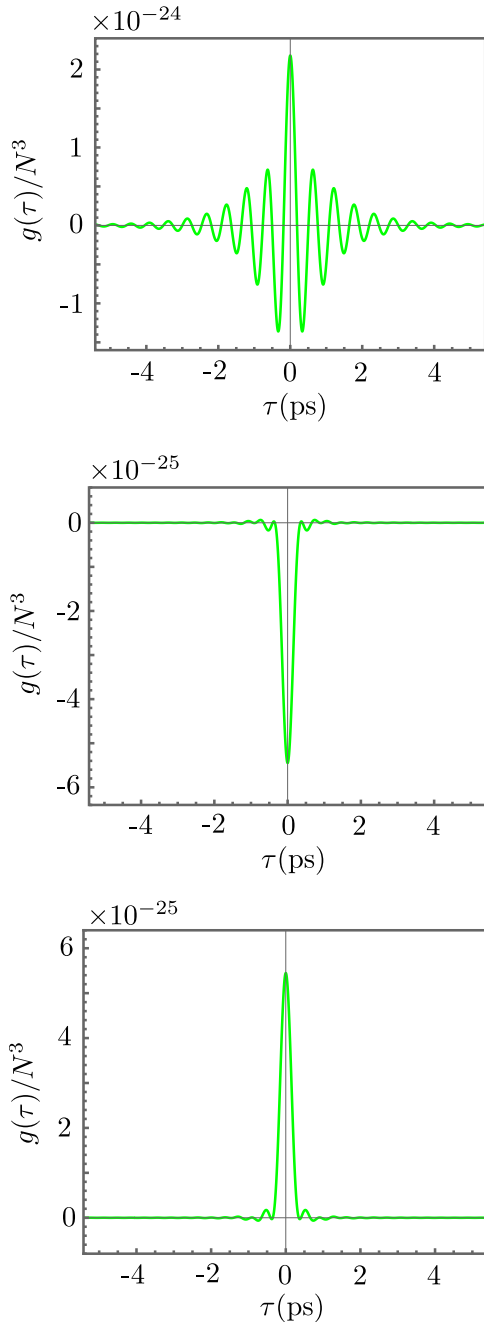
FIG. 6. Top: $V_{\{1,3\}}^{(a)}(\tau)/N^3$. Bottom: $V_{\{1,3\}}^{(b)}(\tau)/N^3$.

FIG. 5. Top: $V_{\{2,2\}}^{(a)}(\tau)/N^3$. Center: $V_{\{2,2\}}^{(b)}(\tau)/N^3$. Bottom: $V_{\{2,2\}}^{(c)}(\tau)/N^3$.

$$V_{\{0,4\}}^{(b)}(\tau) = \frac{C_2}{\sqrt{5}} \sum_{t=\pm} \sum_{i=1,2} \int_{-\infty}^{\infty} d\Omega \int_{-\infty}^{\infty} d\Omega'(\Omega\Omega')$$
$$\times R_0^{(+)*}(\Omega', 0, 0) G_{ii}^{(t,t)}(\Omega, \Omega', \Omega', 0, \tau), \tag{D9}$$

and

$$V_{\{0,4\}}^{(c)}(\tau) = \frac{C_2}{\sqrt{5}} \sum_{t=\pm} \sum_{i=1,2} \int_{-\infty}^{\infty} d\Omega \int_{-\infty}^{\infty} d\Omega'(\Omega\Omega')$$
$$\times R_i^{(+)*}(\Omega', \Omega, \tau) G_{0i}^{(t,+)}(\Omega, \Omega', 0, 0, \tau). \tag{D10}$$

with wave vectors $\mathbf{k}_{\text{ch2}} - \mathbf{k}_{\text{ch1}}' + \mathbf{k}_{\text{ch1}}'' - \mathbf{k}_{\text{ch2}}''' + \mathbf{k}_{\text{ch1}}''$ and $\mathbf{k}_{\text{ch2}}$ (and the corresponding terms with swapped indices). The corresponding expressions are

Because both $V_{\{0,4\}}^{(a)}(\tau)$ and $V_{\{0,4\}}^{(b)}(\tau)$ turn out to vanish on the grounds of symmetry [for the same reason why Eq. (A10) vanishes], $V_{\{0,4\}}^{(c)}(\tau)$ is the only nonvanishing term in this series; its profile is shown in Fig. 7.

$$V_{\{0,4\}}^{(a)}(\tau) = \frac{C_2}{\sqrt{5}} \sum_{t,s=\pm} \int_{-\infty}^{\infty} d\Omega \int_{-\infty}^{\infty} d\Omega'(\Omega\Omega') R_0^{(+)*}(\Omega', 0, 0)$$
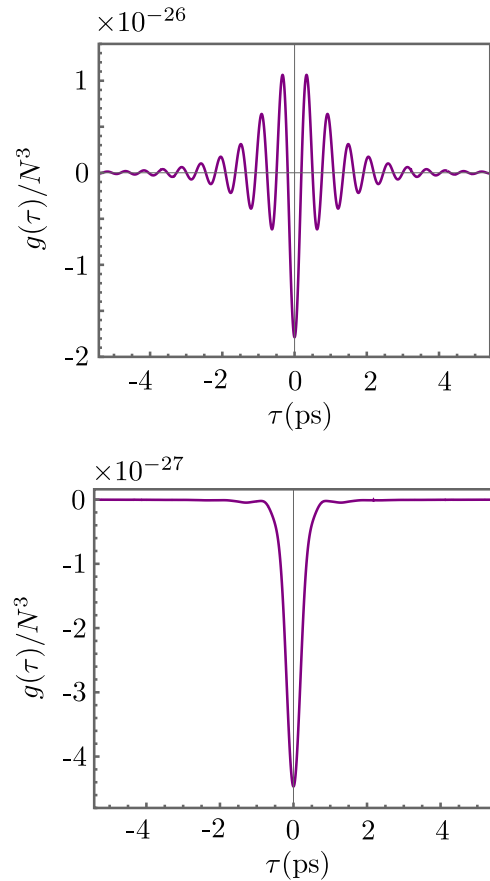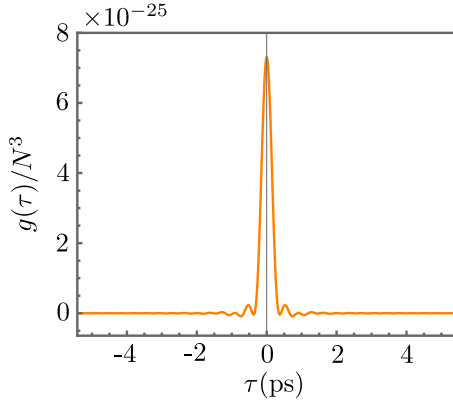$$\times G_{00}^{(t,s)}(\Omega, \Omega', 0, 0, 0)[\cos(\Omega\tau) + \cos(\Omega'\tau)], \tag{D8}$$

There is a minute difference between N_{min} in Fig. 4 and the corresponding N at which the fourth-order contributions to the BA starts to dominate in the two-channel measurement, and it is related to the splitting of each single-channel contribution $\hat{E}_s^{(m)}$ into 2^{m-1} terms when two pulses are present.

FIG. 7. $V_{\{0,4\}}^{(c)}(\tau)/N^3$ profile.

APPENDIX E: PHASE MATCHING, DISPERSION, AND ABSORPTION

For the first set of parameters, the RI in the MIR range up to 150 THz is modeled as [40]

$$n_{\Omega}^{(\mathrm{set1})} = \mathrm{Re}\sqrt{6.7\left[1 + \frac{(6.2)^2 - (5.3)^2}{(5.3)^2 - \widetilde{\Omega}^2 - 0.09i|\widetilde{\Omega}|}\right]}, \quad (\mathrm{E1})$$

where $\widetilde{\Omega} = \Omega/(2\pi \times 10^{12}\,\mathrm{THz})$. The corresponding gating function is shown in Fig. 8. Since an absorption peak is found at around 5 THz, a cutoff is applied for frequencies below 18 THz when calculations involving the first set of parameters are considered.

Consideration of the second set of parameters requires the usage of a different RI profile due to the extra low-frequency band selected by the gating function, partially overlapping with the absorption peak of the medium. In this case, the following dispersion profile is utilized [17]:

$$n_{\Omega} = -0.0164\,\widetilde{\Omega}^6 + 0.1478\left|\widetilde{\Omega}\right|^5 - 0.5185\,\widetilde{\Omega}^4$$
$$+ 0.8974\left|\widetilde{\Omega}\right|^3 - 0.7782\,\widetilde{\Omega}^2 + 0.3283\left|\widetilde{\Omega}\right| + 3.0657. \quad (\mathrm{E2})$$

On top of that, an additional damping function is included in the gating function for the second parameter set in order to account for absorption. The absorption profile (extracted from
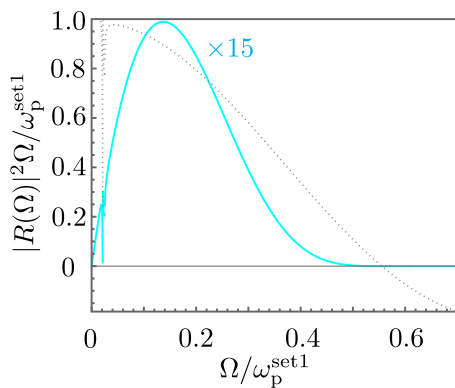

FIG. 8. (Full cyan) Gating function $|R(\Omega)|^2\Omega/\omega_{\mathrm{p}}^{\mathrm{set\,1}}$ for the first set of parameters considered (scaled up by factor 15). (Dotted gray) Corresponding phase-matching function $|\zeta_{\omega,\Omega}|/(d\frac{L\omega}{2c_0 n})$.

FIG. 9. (Full cyan) Gating function $|R(\Omega)|^2\mathrm{Abs}(\Omega)\Omega/\omega_{\mathrm{p}}^{(\mathrm{set\,2})}$ for the second set of parameters considered (scaled up by 1500). (Dotted gray) Corresponding phase-matching function $|\zeta_{\omega,\Omega}|/(d\frac{L\omega}{2c_0 n})$.
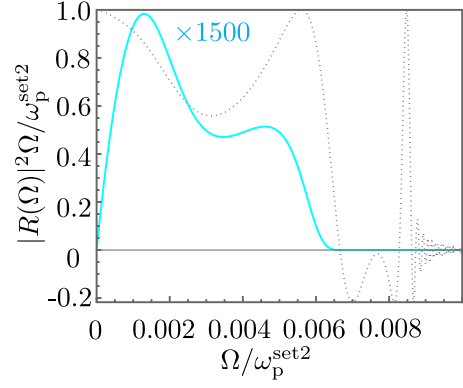
Ref. [17]) is given by

$$\mathrm{Abs}(\Omega) = \exp[-0.000\,618\,\widetilde{\Omega}^8 - 0.000\,087\,9\,\widetilde{\Omega}^6]. \quad (\mathrm{E3})$$

Fortunately, the effect from taking Eq. (E3) into account is marginal, so that the validity of the paraxial quantization is not compromised. This also justifies the neglection of absorption when treating the two-channel experiment, in order to decrease computational effort. The resulting phase-matching function (including absorption) is shown in Fig. 9.

APPENDIX F: $\chi^{(3)}$ CONTRIBUTION

An aspect that might arise when accounting for cascaded nonlinear processes is the possibility of four-wave mixing taking place. The main contribution to the nonlinear polarization leading to the generation of such field components is proportional to the susceptibility $\chi^{(3)}$ and to the combination of terms $E_{\mathrm{p}}^2(t)\delta\hat{E}(t)$. Under the assumption of Kleinman symmetry [29], there are six $\chi^{(3)}$ components that can generate measurable field components: $\chi_{xxzz}^{(3)} = \chi_{yyzz}^{(3)}$, $\chi_{xzxz}^{(3)} = \chi_{yzyz}^{(3)}$, and $\chi_{xzzx}^{(3)} = \chi_{yzzy}^{(3)}$. In fact, for a probe pulse propagating through a ZnTe crystal along the [110] direction and polarized along the [001] axis, the (third-order) nonlinear-polarization components generating additional electric fields are

$$\hat{P}_x^{(3)}(t) = \epsilon_0(\chi_{xxzz}^{(3)} + \chi_{xzxz}^{(3)} + \chi_{xzzx}^{(3)})E_{\mathrm{p}}^2(t)\delta\hat{E}_x(t) \quad (\mathrm{F1})$$

and

$$\hat{P}_y^{(3)}(t) = \epsilon_0(\chi_{yyzz}^{(3)} + \chi_{yzyz}^{(3)} + \chi_{yzzy}^{(3)})E_{\mathrm{p}}^2(t)\delta\hat{E}_y(t). \quad (\mathrm{F2})$$

In terms of the basis spanned by $\mathbf{e}_z$, $\mathbf{e}_s$, and $\mathbf{e}_k$, this polarization has a longitudinal $\mathbf{e}_k$ component, which does not generate any outgoing field contribution, and a $\mathbf{e}_s$ component

$$\hat{P}_s^{(3)}(t) = \epsilon_0(\chi_{xxzz}^{(3)} + \chi_{xzxz}^{(3)} + \chi_{xzzx}^{(3)})E_{\mathrm{p}}^2(t)\delta\hat{E}_s(t), \quad (\mathrm{F3})$$

with $\delta\hat{E}_s = \frac{1}{\sqrt{2}}(\delta\hat{E}_y - \delta\hat{E}_x)$. For brevity, we denote $X = \chi_{xxzz}^{(3)} + \chi_{xzxz}^{(3)} + \chi_{xzzx}^{(3)}$. From our definition, the spectral decom-

position of this expression gives

$$P_s^{(3)}(\omega) = \epsilon_0 X \int_{-\infty}^{\infty} d\omega' I(\omega - \omega') \delta \hat{E}_s(\omega')$$

$$\times e^{\frac{ir_k}{c_0}[\omega' n_{\omega'} + (\omega - \omega') n_{\omega - \omega'} - \omega n_\omega]}, \quad \text{(F4)}$$

in which

$$I(\Omega) = \int_{-\infty}^{\infty} d\omega \, E_p^*(\omega - \Omega) E_p(\omega) e^{\frac{ir_k}{c_0}[\omega n_\omega - (\omega - \Omega) n_{\omega - \Omega} - \Omega n_\Omega]}. \quad \text{(F5)}$$

With this polarization, we find the following approximate solution to the paraxial equation:

$$\hat{E}_s^{\chi^{(3)}}(\omega) = \frac{XL\omega}{2nc_0} \int_{-\infty}^{\infty} d\omega' d\omega'' E_p^*(\omega' + \omega'' - \omega) E_p(\omega') \delta \hat{E}_s(\omega'') \operatorname{sinc}\left\{\frac{L}{2c_0}[\omega'' n_{\omega''} - (\omega' + \omega'' - \omega) n_{\omega' + \omega'' - \omega} - \omega n_\omega + \omega' n_{\omega'}]\right\}. \quad \text{(F6)}$$

When all the three frequencies in Eq. (F6) are in the NIR, $\operatorname{sinc}\{\frac{L}{2c_0}[\omega'' n_{\omega''} - (\omega' + \omega'' - \omega) n_{\omega' + \omega'' - \omega} - \omega n_\omega + \omega' n_{\omega'}]\} \approx 1$. This allows one to write the signal operator resulting after the ellipsometry step as (note that even though the spatial argument of the electric field has been omitted, the effect of the beam waist is accounted for in the value of $A^{(3)}$ used for the signal operator)

$$\hat{S}^{\chi^{(3)}} = \frac{4\sqrt{\epsilon_0} X L \kappa i}{w_0^2 \sqrt{3\pi \hbar c_0 n}} \int_0^{\infty} d\omega \int_{-\infty}^{\infty} d\omega' \sqrt{\omega'}$$

$$\times \sqrt{\frac{n}{n_{\omega'}}} F(\omega' - \omega) \alpha_p^*(\omega) \hat{a}(\omega') + \text{H.c.} \quad \text{(F7)}$$

Equation (F7) does not give any contributions at second order since its cross term with $\hat{S}^{(0)}$ vanishes. At fourth order, only the square of Eq. (F7) contributes and gives

$$\langle [\hat{S}^{\chi^{(3)}}]^2 \rangle = \frac{4N^3}{3} \left(\frac{L\omega_p}{nc_0} X\right)^2 \left(\frac{\hbar}{4\pi^2 \epsilon_0 c_0 n w_0^2}\right)^2 \int_0^{\infty} d\omega \int_0^{\infty} d\omega'$$

$$\times \int_0^{\infty} d\omega'' \frac{n}{n_{\omega'}} \omega' F(\omega' - \omega) F^*(\omega' - \omega'')$$

$$\times \frac{\alpha_p^*(\omega) \alpha_p(\omega'')}{\beta}. \quad \text{(F8)}$$

Precise values of the relevant tensor components of $\chi^{(3)}$ cannot, to the best of our knowledge, be found reliably in the literature. Indirect $\chi^{(3)}$ measurements based on the RI modulation through Kerr effect lead to a wide span of reported values [41–44]. The large fluctuations in the found values for linear combinations of $\chi^{(3)}$ tensor components can be traced back to the sampled frequency ranges, with measurements near the two-photon-absorption frequency (when the sum of the frequencies of two photons matches the band gap of the NX) leading to resonantly enhanced values of the third-order nonlinear susceptibility. At such frequencies, undesired effects like crystal heating (through generation of electron-hole pairs) and probe depletion might take place. For ZnTe, used in Ref. [17], the band gap corresponds to a frequency of $\Delta\omega \approx 550$ THz, while for AgGaS$_2$, used in Ref. [10], the value is $\Delta\omega \approx 660$ THz. Adopting the $\chi^{(3)}$ value extracted from Ref. [43] and assuming all tensor components in X to be the same, one arrives at $\langle [\hat{S}^{\chi^{(3)}}]^2 \rangle \sim 10^{-21} N^3$ for the first set of parameters. $\langle [\hat{S}^{\chi^{(3)}}]^2 \rangle$ might be as large as (or possibly larger than) the signal-variance contributions originating from cascaded $\chi^{(2)}$ processes (depending on the choice of NX and probe frequency range). The contribution described by Eq. (F8), however, relates to a process of nature similar to self-phase modulation and therefore affects solely the electric-field fluctuations in the probe pulse (SN enhancement). These $\chi^{(3)}$ contributions have no connections to the sampled MIR vacuum and can be suppressed in a measurement (e.g., by investigating and avoiding the presence of self-phase modulation in the spectrum of the probe pulse), therefore justifying their neglection in our paper.

APPENDIX G: QUANTUM-STATE EVOLUTION

The quantum states participating in EO sampling involve two polarizations and an ultrabroad-band continuous range of frequencies. The treatment of a multimode problem can be circumvented by the use of nonmonochromatic modes covering the involved NIR and the MIR frequency ranges, leading to an effective description of the probe-driven interaction as a two-mode squeezing between the s-polarized MIR and NIR modes [22]. In the subcycle sampling regime, the corresponding nonmonochromatic mode operators exhibit some unusual properties that can be related to the presence of virtual particles. As an example, the MIR annihilation operator does not completely annihilate the vacuum state $|\{0\}_\Omega\rangle$ defined over the continuous set of the MIR frequencies. For the sake of simplicity, we shall ignore these properties. If we additionally adopt a fully quantum description of the probe, the state evolution can then be treated in terms of an effective three-mode interaction, with corresponding operators $\hat{a}_{\text{MIR}}$, $\hat{a}_{\text{NIR}}$, and $\hat{a}_p$ for the s-polarized MIR, s-polarized NIR, and z-polarized NIR (probe), respectively. One can then enforce energy conservation on the Hamiltonian (neglecting time-ordering effects) and exclude up-conversion to frequencies above the NIR (as well as the inverse process), so that the simplified action $\hat{S} = \int dt \hat{H}$ becomes

$$\hat{S} = A \hat{a}_{\text{MIR}}^\dagger \hat{a}_{\text{NIR}}^\dagger \hat{a}_p + A^* \hat{a}_{\text{MIR}} \hat{a}_{\text{NIR}} \hat{a}_p^\dagger + C \hat{a}_{\text{MIR}} \hat{a}_{\text{NIR}}^\dagger \hat{a}_p + C^* \hat{a}_{\text{MIR}}^\dagger \hat{a}_{\text{NIR}} \hat{a}_p^\dagger \quad \text{(G1)}$$

and the unitary evolution operator reads as

$$\hat{U} = \exp\{\mathcal{A}\hat{a}^\dagger_{\text{MIR}}\hat{a}^\dagger_{\text{NIR}}\hat{a}_{\text{p}} - \mathcal{A}^*\hat{a}_{\text{MIR}}\hat{a}_{\text{NIR}}\hat{a}^\dagger_{\text{p}} + \mathcal{C}\hat{a}_{\text{MIR}}\hat{a}^\dagger_{\text{NIR}}\hat{a}_{\text{p}} - \mathcal{C}^*\hat{a}^\dagger_{\text{MIR}}\hat{a}_{\text{NIR}}\hat{a}^\dagger_{\text{p}}\}, \tag{G2}$$

with $\mathcal{A} = -iA$ and $\mathcal{C} = -iC$ being coefficients depending on the field quantization considered and on the properties, geometry, and modeling of the NX (so that $\mathcal{A}$ and $\mathcal{C}$ are proportional to linear combinations of elements of the nonlinear susceptibility). If for all three considered modes neither annihilation nor creation is favored relative to each other (what could happen, e.g., by considering frequencies close to the NX resonance), $|A| = |C|$ holds.

For the EO sampling, we consider the input state $|\alpha, 0, 0\rangle$, where the first, second, and third entries stand for the probe (z-polarized NIR mode), MIR, and s-polarized NIR modes, respectively. The probe is initially in the coherent state of amplitude α generated by a corresponding displacement operator, while both the MIR and s-polarized NIR modes are in their vacuum states. Through Taylor expansion, the first-order correction to the initial state caused by Eq. (G2) is given by

$$|\text{out}_1\rangle = \ln\hat{U}|\alpha, 0, 0\rangle = \mathcal{A}\alpha|\alpha, 1, 1\rangle, \tag{G3}$$

while the second-order one reads as

$$|\text{out}_2\rangle = \frac{1}{2}\ln^2\hat{U}|\alpha, 0, 0\rangle = \left(\mathcal{A}^2\alpha^2|\alpha, 2, 2\rangle - \frac{1}{2}|\mathcal{A}|^2\alpha\hat{a}^\dagger_{\text{p}}|\alpha, 0, 0\rangle + \frac{1}{\sqrt{2}}\mathcal{A}\mathcal{C}\alpha^2|\alpha, 0, 2\rangle - \frac{1}{\sqrt{2}}\mathcal{A}\mathcal{C}^*\alpha\hat{a}^\dagger_{\text{p}}|\alpha, 2, 0\rangle\right). \tag{G4}$$

The conjunction of quarter-wave plate, Wollaston prism, and photon detection leads to the signal operator

$$\hat{S} = i(\hat{a}^\dagger_{\text{p}}\hat{a}_{\text{NIR}} - \hat{a}^\dagger_{\text{NIR}}\hat{a}_{\text{p}}), \tag{G5}$$

which can be applied on (G3) and (G4) to give

$$|\text{sig}_1\rangle = \hat{S}|\text{out}_1\rangle = i\mathcal{A}\alpha(\hat{a}^\dagger_{\text{p}}|\alpha, 1, 0\rangle - \sqrt{2}\alpha|\alpha, 1, 2\rangle) \tag{G6}$$

and

$$|\text{sig}_2\rangle = \hat{S}|\text{out}_2\rangle = i\left[\sqrt{2}\mathcal{A}^2\alpha^2\hat{a}^\dagger_{\text{p}}|\alpha, 2, 1\rangle - \sqrt{3}\mathcal{A}^2\alpha^3|\alpha, 2, 3\rangle + \frac{1}{2}|\mathcal{A}|^2\alpha(\hat{a}^\dagger_{\text{p}}\alpha + 1)|\alpha, 0, 1\rangle + \mathcal{A}\mathcal{C}\alpha^2\hat{a}^\dagger_{\text{p}}|\alpha, 0, 1\rangle\right.$$
$$\left. - \sqrt{\frac{3}{2}}\mathcal{A}\mathcal{C}\alpha^3|\alpha, 0, 3\rangle + \frac{1}{\sqrt{2}}\mathcal{A}\mathcal{C}^*\alpha(\hat{a}^\dagger_{\text{p}}\alpha + 1)|\alpha, 2, 1\rangle\right]. \tag{G7}$$

Together with

$$|\text{sig}_0\rangle = \hat{S}|\alpha, 0, 0\rangle = -i\alpha|\alpha, 0, 1\rangle, \tag{G8}$$

which gives the (shot-noise) contribution $\langle\text{sig}_0|\text{sig}_0\rangle = |\alpha|^2$, and $\langle\hat{S}\rangle = 0$, the expectation value for the signal variance up to the second order is given by $\langle\hat{S}^2\rangle = \langle\text{sig}_0|\text{sig}_0\rangle + \langle\text{sig}_1|\text{sig}_1\rangle + \langle\text{sig}_0|\text{sig}_2\rangle + \langle\text{sig}_2|\text{sig}_0\rangle$, with

$$\langle\text{sig}_1|\text{sig}_1\rangle = |\mathcal{A}|^2|\alpha|^2(1 + 3|\alpha|^2) \tag{G9}$$

and

$$\langle\text{sig}_0|\text{sig}_2\rangle + \langle\text{sig}_2|\text{sig}_0\rangle = -|\mathcal{A}|^2|\alpha|^2 - (|\mathcal{A}|^2 + \mathcal{A}\mathcal{C} + \mathcal{A}^*\mathcal{C}^*)|\alpha|^4. \tag{G10}$$

In other words, the total signal variance takes the form

$$\langle\hat{S}^2\rangle = |\alpha|^2 + (2|\mathcal{A}|^2 - \mathcal{A}\mathcal{C} - \mathcal{A}^*\mathcal{C}^*)|\alpha|^4, \tag{G11}$$

where the EO term is proportional to $|\alpha|^4 \propto N^2$. Note that $|\text{out}_1\rangle$ (which has the same MIR state as $|\text{sig}_1\rangle$) contains a MIR photon, while $|\text{out}_2\rangle$ contains contributions from states both with and without MIR photons, but only the latter contribute to the signal at second order. It is insightful to reconnect this state-evolution approach to the Heisenberg-picture calculations presented in this paper. One can notice that $\langle\text{sig}_1|\text{sig}_1\rangle$ and $\langle\text{sig}_0|\text{sig}_2\rangle + \langle\text{sig}_2|\text{sig}_0\rangle$ are related to both $\langle\alpha, 0, 0|[\hat{S}^{(1)}]^2|\alpha, 0, 0\rangle = \langle[\hat{S}^{(1)}]^2\rangle$ [the superscript (1) here denotes first-order operator evolution, as in the main text] and $\langle\hat{S}^{(2)}\hat{S}^{(0)}\rangle + \langle\hat{S}^{(0)}\hat{S}^{(2)}\rangle$ since

$$\langle[\hat{S}^{(1)}]^2\rangle = \langle[\hat{S}, \ln\hat{U}]^2\rangle = -\langle\ln\hat{U}\hat{S}^2\ln\hat{U}\rangle + \langle[\ln\hat{U}\hat{S}]^2\rangle - \langle\hat{S}\ln^2\hat{U}\hat{S}\rangle + \langle[\hat{S}\ln\hat{U}]^2\rangle \tag{G12}$$

and

$$\langle\{\hat{S}^{(2)}, \hat{S}^{(0)}\}\rangle = \frac{1}{2}\langle[[\hat{S}, \ln\hat{U}], \ln\hat{U}]\hat{S}\rangle + \frac{1}{2}\langle\hat{S}[[\hat{S}, \ln\hat{U}], \ln\hat{U}]\rangle = \frac{1}{2}\langle\ln^2\hat{U}\hat{S}^2\rangle + \frac{1}{2}\langle\hat{S}^2\ln^2\hat{U}\rangle - \langle[\ln\hat{U}\hat{S}]^2\rangle$$
$$+ \langle\hat{S}\ln^2\hat{U}\hat{S}\rangle - \langle[\hat{S}\ln\hat{U}]^2\rangle. \tag{G13}$$

When combining Eqs. (G12) and (G13), the terms that do not lead to either $\langle\text{sig}_1|\text{sig}_1\rangle$ or $\langle\text{sig}_0|\text{sig}_2\rangle + \langle\text{sig}_2|\text{sig}_0\rangle$ mutually cancel. Note that $\ln\hat{U}$ is anti-Hermitian, so that $\langle\text{out}_1| = -\langle\alpha, 0, 0|\ln\hat{U}$ and therefore $\langle[\hat{S}^{(1)}]^2\rangle + \langle\hat{S}^{(2)}\hat{S}^{(0)}\rangle + \langle\hat{S}^{(0)}\hat{S}^{(2)}\rangle = \langle\text{sig}_1|\text{sig}_1\rangle + \langle\text{sig}_0|\text{sig}_2\rangle + \langle\text{sig}_2|\text{sig}_0\rangle$. The terms that mutually cancel, however, are still present in the evolved signals and result in contributions to the signal variance arising from $\hat{S}^{(1)}$ and $\hat{S}^{(2)}$ that carry contributions from both $|\text{sig}_1\rangle$ and $|\text{sig}_2\rangle$.

Explicit evolution of the signal operator (G5) results in

$$\hat{\mathcal{S}}^{(1)} = -i[\hat{n}_{\mathrm{p}} - \hat{n}_{\mathrm{NIR}}][(\mathcal{A} - \mathcal{C}^*)\hat{a}_{\mathrm{MIR}}^\dagger - (\mathcal{A}^* - \mathcal{C})\hat{a}_{\mathrm{MIR}}] \tag{G14}$$

and

$$\begin{aligned}\hat{\mathcal{S}}^{(2)} =& \frac{i}{2}(|\mathcal{A}|^2 - |\mathcal{C}|^2)[\hat{n}_{\mathrm{p}} - \hat{n}_{\mathrm{NIR}}][\hat{a}_{\mathrm{p}}^\dagger\hat{a}_{\mathrm{NIR}} - \hat{a}_{\mathrm{NIR}}^\dagger\hat{a}_{\mathrm{p}}] \\ & - i[\mathcal{A}\hat{a}_{\mathrm{MIR}}^\dagger\hat{a}_{\mathrm{NIR}}^\dagger\hat{a}_{\mathrm{p}} + \mathcal{A}^*\hat{a}_{\mathrm{MIR}}\hat{a}_{\mathrm{NIR}}\hat{a}_{\mathrm{p}}^\dagger + \mathcal{C}\hat{a}_{\mathrm{MIR}}\hat{a}_{\mathrm{NIR}}^\dagger\hat{a}_{\mathrm{p}} + \mathcal{C}^*\hat{a}_{\mathrm{MIR}}^\dagger\hat{a}_{\mathrm{NIR}}\hat{a}_{\mathrm{p}}^\dagger][(\mathcal{A} - \mathcal{C}^*)\hat{a}_{\mathrm{MIR}}^\dagger - (\mathcal{A}^* - \mathcal{C})\hat{a}_{\mathrm{MIR}}]. \end{aligned} \tag{G15}$$

It is worth mentioning that by considering in this paper only nested convolutions linear in the unperturbed quantum fields $\delta\hat{E}$, we are keeping solely the terms proportional to $\hat{n}_{\mathrm{p}} = \hat{a}_p^\dagger\hat{a}_p$ in the above equations. These are the terms that give the $|\alpha|^4$ contributions to the signal variances.

Using Eq. (G15), one can calculate

$$\begin{aligned}\{\hat{\mathcal{S}}^{(0)}, \hat{\mathcal{S}}^{(2)}\} =& -(|\mathcal{A}|^2 - |\mathcal{C}|^2)\{\hat{n}_{\mathrm{p}}(\hat{n}_{\mathrm{NIR}} + 1) - \hat{n}_{\mathrm{NIR}}(\hat{n}_{\mathrm{p}} + 1) - (\hat{a}_{\mathrm{p}}^\dagger)^2\hat{a}_{\mathrm{NIR}}^2 + (\hat{a}_{\mathrm{NIR}}^\dagger)^2\hat{a}_{\mathrm{p}}^2 \\ & + [\hat{n}_{\mathrm{p}} - \hat{n}_{\mathrm{NIR}}][-\hat{n}_{\mathrm{p}}(\hat{n}_{\mathrm{NIR}} + 1) - \hat{n}_{\mathrm{NIR}}(\hat{n}_{\mathrm{p}} + 1) + (\hat{a}_{\mathrm{p}}^\dagger)^2\hat{a}_{\mathrm{NIR}}^2 - (\hat{a}_{\mathrm{NIR}}^\dagger)^2\hat{a}_{\mathrm{p}}^2]\} \\ & + \{2[\mathcal{A}\hat{a}_{\mathrm{MIR}}^\dagger\hat{a}_{\mathrm{NIR}}^\dagger\hat{a}_{\mathrm{p}} + \mathcal{A}^*\hat{a}_{\mathrm{MIR}}\hat{a}_{\mathrm{NIR}}\hat{a}_{\mathrm{p}}^\dagger + \mathcal{C}\hat{a}_{\mathrm{MIR}}\hat{a}_{\mathrm{NIR}}^\dagger\hat{a}_{\mathrm{p}} + \mathcal{C}^*\hat{a}_{\mathrm{MIR}}^\dagger\hat{a}_{\mathrm{NIR}}\hat{a}_{\mathrm{p}}^\dagger](\hat{a}_{\mathrm{p}}^\dagger\hat{a}_{\mathrm{NIR}} - \hat{a}_{\mathrm{NIR}}^\dagger\hat{a}_{\mathrm{p}}) \\ & + (\hat{n}_{\mathrm{p}} - \hat{n}_{\mathrm{NIR}})[(\mathcal{A} + \mathcal{C}^*)\hat{a}_{\mathrm{MIR}}^\dagger + (\mathcal{A}^* + \mathcal{C})\hat{a}_{\mathrm{MIR}}]\}[(\mathcal{A} - \mathcal{C}^*)\hat{a}_{\mathrm{MIR}}^\dagger - (\mathcal{A}^* - \mathcal{C})\hat{a}_{\mathrm{MIR}}], \end{aligned} \tag{G16}$$

which leads to

$$\langle\{\hat{\mathcal{S}}^{(2)}, \hat{\mathcal{S}}^{(0)}\}\rangle = -(|\mathcal{A}|^2 + |\mathcal{C}|^2 - \mathcal{A}\mathcal{C} - \mathcal{A}^*\mathcal{C}^*)|\alpha|^2 + (|\mathcal{A}|^2 - |\mathcal{C}|^2)|\alpha|^4. \tag{G17}$$

Similarly,

$$\langle[\hat{\mathcal{S}}^{(1)}]^2\rangle = (|\mathcal{A}|^2 + |\mathcal{C}|^2 - \mathcal{A}\mathcal{C} - \mathcal{A}^*\mathcal{C}^*)(|\alpha|^2 + |\alpha|^4). \tag{G18}$$

It is clear that the above equations are linear combinations of (G9) and (G10), emphasizing the fact that both $\langle\hat{\mathcal{S}}^{(2)}\hat{\mathcal{S}}^{(0)}\rangle + \langle\hat{\mathcal{S}}^{(0)}\hat{\mathcal{S}}^{(2)}\rangle$ and $\langle[\hat{\mathcal{S}}^{(1)}]^2\rangle$ contain contributions from populated MIR states. When the relation $|A| = |C|$ holds, the $|\alpha|^4$-dependent term in $\langle\hat{\mathcal{S}}^{(2)}\hat{\mathcal{S}}^{(0)}\rangle + \langle\hat{\mathcal{S}}^{(0)}\hat{\mathcal{S}}^{(2)}\rangle$ vanishes, in agreement with Eq. (A2).

For a two-channel setup, similar calculations can be performed using the initial state $|\alpha_{\mathrm{ch1}}, \alpha_{\mathrm{ch2}}, 0_{\mathrm{MIR}}, 0_{\mathrm{NIR,ch1}}, 0_{\mathrm{NIR,ch2}}\rangle$. The signal operator has to be replaced by two operators: $\hat{\mathcal{S}}_{\mathrm{ch1}} = i(\hat{a}_{\mathrm{p,ch1}}^\dagger\hat{a}_{\mathrm{NIR,ch1}} - \hat{a}_{\mathrm{NIR,ch1}}^\dagger\hat{a}_{\mathrm{p,ch1}})$ and $\hat{\mathcal{S}}_{\mathrm{ch2}} = i(\hat{a}_{\mathrm{p,ch2}}^\dagger\hat{a}_{\mathrm{NIR,ch2}} - \hat{a}_{\mathrm{NIR,ch2}}^\dagger\hat{a}_{\mathrm{p,ch2}})$. Analogously, in the evolution operator in place of $\mathcal{A}\hat{a}_{\mathrm{p}}\hat{a}_{\mathrm{NIR}}^\dagger\hat{a}_{\mathrm{MIR}}^\dagger$ one should consider $\mathcal{A}_{\mathrm{ch1}}\hat{a}_{\mathrm{p,ch1}}\hat{a}_{\mathrm{NIR,ch1}}^\dagger\hat{a}_{\mathrm{MIR}}^\dagger + \mathcal{A}_{\mathrm{ch2}}\hat{a}_{\mathrm{p,ch2}}\hat{a}_{\mathrm{NIR,ch2}}^\dagger\hat{a}_{\mathrm{MIR}}^\dagger$ $[\hat{a}_{\mathrm{MIR}} = (\hat{a}_{\mathrm{MIR,ch1}} + i\hat{a}_{\mathrm{MIR,ch2}})/\sqrt{2}]$, with similar replacements for the other terms. This can be clearly seen, e.g., for the first-order state

$$|\mathrm{out}_1'\rangle = \mathcal{A}_{\mathrm{ch1}}\alpha_{\mathrm{ch1}}|\alpha_{\mathrm{ch1}}, \alpha_{\mathrm{ch2}}, 1, 1, 0\rangle + \mathcal{A}_{\mathrm{ch2}}\alpha_{\mathrm{ch2}}|\alpha_{\mathrm{ch1}}, \alpha_{\mathrm{ch2}}, 1, 0, 1\rangle, \tag{G19}$$

which can generate two contributions

$$|\mathrm{sig}_{1,\mathrm{ch1}}'\rangle = i\mathcal{A}_{\mathrm{ch1}}\alpha_{\mathrm{ch1}}\hat{a}_{\mathrm{p,ch1}}^\dagger|\alpha_{\mathrm{ch1}}, \alpha_{\mathrm{ch2}}, 1, 0, 0\rangle - i\sqrt{2}\mathcal{A}_{\mathrm{ch1}}\alpha_{\mathrm{ch1}}^2|\alpha_{\mathrm{ch1}}, \alpha_{\mathrm{ch2}}, 1, 2, 0\rangle - i\mathcal{A}_{\mathrm{ch2}}\alpha_{\mathrm{ch1}}\alpha_{\mathrm{ch2}}|\alpha_{\mathrm{ch1}}, \alpha_{\mathrm{ch2}}, 1, 1, 1\rangle \tag{G20}$$

and

$$|\mathrm{sig}_{1,\mathrm{ch2}}'\rangle = i\mathcal{A}_{\mathrm{ch2}}\alpha_{\mathrm{ch2}}\hat{a}_{\mathrm{p,ch2}}^\dagger|\alpha_{\mathrm{ch1}}, \alpha_{\mathrm{ch2}}, 1, 0, 0\rangle - i\sqrt{2}\mathcal{A}_{\mathrm{ch2}}\alpha_{\mathrm{ch2}}^2|\alpha_{\mathrm{ch1}}, \alpha_{\mathrm{ch2}}, 1, 0, 2\rangle - i\mathcal{A}_{\mathrm{ch1}}\alpha_{\mathrm{ch1}}\alpha_{\mathrm{ch2}}|\alpha_{\mathrm{ch1}}, \alpha_{\mathrm{ch2}}, 1, 1, 1\rangle. \tag{G21}$$

The cross-signal contribution to the variance (relevant for the corresponding experiment) then reads

$$\langle\mathrm{sig}_{1,\mathrm{ch1}}'|\mathrm{sig}_{1,\mathrm{ch2}}'\rangle + \langle\mathrm{sig}_{1,\mathrm{ch2}}'|\mathrm{sig}_{1,\mathrm{ch1}}'\rangle = 2(\mathcal{A}_{\mathrm{ch1}}^*\mathcal{A}_{\mathrm{ch2}} + \mathcal{A}_{\mathrm{ch1}}\mathcal{A}_{\mathrm{ch2}}^*)|\alpha_{\mathrm{ch1}}\alpha_{\mathrm{ch2}}|^2. \tag{G22}$$

The other second-order term gives

$$\begin{aligned}\langle\mathrm{sig}_{0,\mathrm{ch1}}'|\mathrm{sig}_{2,\mathrm{ch2}}'\rangle & + \langle\mathrm{sig}_{2,\mathrm{ch2}}'|\mathrm{sig}_{0,\mathrm{ch1}}'\rangle + \langle\mathrm{sig}_{2,\mathrm{ch1}}'|\mathrm{sig}_{0,\mathrm{ch2}}'\rangle + \langle\mathrm{sig}_{0,\mathrm{ch2}}'|\mathrm{sig}_{2,\mathrm{ch1}}'\rangle \\ & = -(\mathcal{A}_{\mathrm{ch1}}\mathcal{C}_{\mathrm{ch2}} + \mathcal{A}_{\mathrm{ch2}}\mathcal{C}_{\mathrm{ch1}} + \mathcal{A}_{\mathrm{ch1}}^*\mathcal{C}_{\mathrm{ch2}}^* + \mathcal{A}_{\mathrm{ch2}}^*\mathcal{C}_{\mathrm{ch1}}^*)|\alpha_{\mathrm{ch1}}\alpha_{\mathrm{ch2}}|^2. \end{aligned} \tag{G23}$$

Note that these results are different from the corresponding ones for a single channel (in the sense that one cannot recover the latter by simply setting $\alpha_{\mathrm{ch1}} = \alpha_{\mathrm{ch2}}$).

Since the calculations in this section serve a merely illustrative purpose, we shall refrain from going to fourth order here. It is worth noting, however, that these results are expected from the complete calculations shown in the paper in the limit of a gating function proportional to a Dirac delta distribution in frequency.

[1] W. Heisenberg, Über den anschaulichen Inhalt der quanten-theoretischen Kinematik und Mechanik, in *Original Scientific Papers Wissenschaftliche Originalarbeiten*, edited by W. Blum, H. Rechenberg, and H.-P. Dürr (Springer, Berlin, 1985), pp. 478–504.

[2] H. P. Robertson, The Uncertainty Principle, Phys. Rev. **34**, 163 (1929).

[3] R. F. Werner and T. Farrelly, Uncertainty from Heisenberg to Today, Found. Phys. **49**, 460 (2019).

[4] F. Schlawin, J. Phys. B At. Mol. Opt. Phys. **50**, 203001 (2017).

[5] C. H. Bennett and D. P. DiVincenzo, Quantum information and computation, Nature (London) **404**, 247 (2000).

[6] V. B. Braginskii and F. Y. Khalili, *Quantum Measurement* (Cambridge University Press, New York, 1995).

[7] B. M. Terhal, Quantum error correction for quantum memories, Rev. Mod. Phys. **87**, 307 (2015).

[8] H. J. Briegel, D. E. Browne, W. Dür, R. Raussendorf, and M. Van den Nest, Measurement-based quantum computation, Nat. Phys. **5**, 19 (2009).

[9] A. H. Safavi-Naeini, J. Chan, J. T. Hill, T. P. M. Alegre, A. Krause, and O. Painter, Observation of Quantum Motion of a Nanomechanical Resonator, Phys. Rev. Lett. **108**, 033602 (2012).

[10] C. Riek, D. V. Seletskiy, A. S. Moskalenko, J. F. Schmidt, P. Krauspe, S. Eckart, S. Eggert, G. Burkard, and A. Leitenstorfer, Direct sampling of electric-field vacuum fluctuations, Science **350**, 420 (2015).

[11] C. Riek, P. Sulzer, M. Seeger, A. S. Moskalenko, G. Burkard, D. V. Seletskiy, and A. Leitenstorfer, Subcycle quantum electrodynamics, Nature (London) **541**, 376 (2017).

[12] I.-C. Benea-Chelmus, C. Bonzon, C. Maissen, G. Scalari, M. Beck, and J. Faist, Subcycle measurement of intensity correlations in the terahertz frequency range, Phys. Rev. A **93**, 043812 (2016).

[13] F. Y. Khalili, H. Miao, H. Yang, A. H. Safavi-Naeini, O. Painter, and Y. Chen, Quantum back-action in measurements of zero-point mechanical oscillations, Phys. Rev. A **86**, 033840 (2012).

[14] N. Spethmann, J. Kohler, S. Schreppler, L. Buchmann, and D. M. Stamper-Kurn, Cavity-mediated coupling of mechanical oscillators limited by quantum back-action, Nat. Phys. **12**, 27 (2016).

[15] M. Aspelmeyer, T. J. Kippenberg, and F. Marquardt, Cavity optomechanics, Rev. Mod. Phys. **86**, 1391 (2014).

[16] C. B. Møller, R. A. Thomas, G. Vasilakis, E. Zeuthen, Y. Tsaturyan, M. Balabas, K. Jensen, A. Schliesser, K. Hammerer, and E. S. Polzik, Quantum back-action-evading measurement of motion in a negative mass reference frame, Nature (London) **547**, 191 (2017).

[17] I.-C. Benea-Chelmus, F. F. Settembrini, G. Scalari, and J. Faist, Electric field correlation measurements on the electromagnetic vacuum state, Nature (London) **568**, 202 (2019).

[18] Y. Shi, S. Greenfield, and A. K. Pattanayak, Measurement backaction control of quantum dissipation in a nonlinear cavity-based Duffing oscillator, Phys. Rev. A **103**, 052212 (2021).

[19] M. Boissonneault, A. C. Doherty, F. R. Ong, P. Bertet, D. Vion, D. Esteve, and A. Blais, Back-action of a driven nonlinear resonator on a superconducting qubit, Phys. Rev. A **85**, 022305 (2012).

[20] T. L. M. Guedes, M. Kizmann, D. V. Seletskiy, A. Leitenstorfer, G. Burkard, and A. S. Moskalenko, Spectra of Ultrabroadband Squeezed Pulses and the Finite-Time Unruh-Davies Effect, Phys. Rev. Lett. **122**, 053604 (2019).

[21] M. Kizmann, T. L. M. Guedes, D. V. Seletskiy, A. S. Moskalenko, A. Leitenstorfer, and G. Burkard, Subcycle squeezing of light from a time flow perspective, Nat. Phys. **15**, 960 (2019).

[22] S. Onoe, T. L. M. Guedes, A. S. Moskalenko, A. Leitenstorfer, G. Burkard, and T. C. Ralph, Realizing a rapidly switched Unruh-DeWitt detector through electro-optic sampling of the electromagnetic vacuum, Phys. Rev. D **105**, 056023 (2022).

[23] T. G. Philbin, C. Kuklewicz, S. Robertson, S. Hill, F. König, and U. Leonhardt, Fiber-Optical Analog of the Event Horizon, Science **319**, 1367 (2008).

[24] M. Kizmann, A. S. Moskalenko, A. Leitenstorfer, G. Burkard, and S. Mukamel, Quantum Susceptibilities in Time-Domain Sampling of Electric Field Fluctuations, Laser Photonics Rev. **16**, 2100423 (2022).

[25] K. E. Dorfman, F. Schlawin, and S. Mukamel, Nonlinear optical signals and spectroscopy with quantum light, Rev. Mod. Phys. **88**, 045008 (2016).

[26] F. F. Settembrini, F. Lindel, A. M. Herter, S. Y. Buhman, and J. Faist, Detection of quantum-vacuum field correlations outside the light cone, Nat. Commun. **13**, 3383 (2022).

[27] Whereas its level still dictates the required acquisition time in the experiment (see, e.g., the Supplemental Material of [17]).

[28] A. S. Moskalenko, C. Riek, D. V. Seletskiy, G. Burkard, and A. Leitenstorfer, Paraxial Theory of Direct Electro-Optic Sampling of the Quantum Vacuum, Phys. Rev. Lett. **115**, 263601 (2015).

[29] R. W. Boyd, *Nonlinear Optics (Third Edition)* (Academic, Burlington, VT, 2008).

[30] L. Allen, M. W. Beijersbergen, R. J. C. Spreeuw, and J. P. Woerdman, Orbital angular momentum of light and the transformation of Laguerre-Gaussian laser modes, Phys. Rev. A **45**, 8185 (1992).

[31] G. F. Calvo, A. Picón, and E. Bagan, Quantum field theory of photons with orbital angular momentum, Phys. Rev. A **73**, 013805 (2006).

[32] The presented solution is equivalent to evolving the electric-field operator in the Heisenberg picture, as shown in [20]. The corresponding evolution Hamiltonian may be found in [22]. Note that the Heisenberg equation for the generated electric field is also given by Maxwell's equations with the nonlinear polarizations as sources.

[33] F. Lindel, R. Bennett, and S. Y. Buhmann, Theory of polaritonic quantum-vacuum detection, Phys. Rev. A **102**, 041701(R) (2020).

[34] F. Lindel, R. Bennett, and S. Y. Buhmann, Macroscopic quantum electrodynamics approach to nonlinear optics and application to polaritonic quantum-vacuum detection, Phys. Rev. A **103**, 033705 (2021).

[35] For a continuous set of modes parametrized by ζ, one has $|\{0\}_\omega\rangle = \lim_{\Delta\zeta \to 0} \bigotimes_k |0\rangle_{k\Delta\zeta}$. The MIR vacuum state is constructed by having the frequency and polarization as the mode parameter ($\zeta_{s/z} = \Lambda$) and selecting only frequencies in the MIR range for the tensor product.

[36] For similar reasons, if the two beams reach the NX with some displacement between the centers of their waists, making G a function of this displacement, the decay length should be of the same magnitude as the beam waists [17].

[37] Through the Wiener-Khintchine theorem, the main (autocorrelation) term in $G(\tau)$ provides information about the spectrally resolved gating function, i.e., $G(\Omega) \propto \Omega |R(\Omega)|^2/n_\Omega$ [34,38,39]. While $\Omega|R(\Omega)|^2$ reflects the sampled range of frequencies, the gating function can incorporate nonlinear-polarization effects of quantum character through Pockels effect [20,24]. This fact is a consequence of dispersion and similar in effect to a beam splitter carrying vacuum fluctuations from its free port.

[38] N. Wiener, Generalized harmonic analysis, Acta Math. **55**, 117 (1930).

[39] A. Khintchine, Korrelationstheorie der stationären stochastischen Prozesse, Math. Ann. **109**, 604 (1934).

[40] A. Leitenstorfer, S. Hunsche, J. Shah, M. C. Nuss, and W. H. Knox, Detectors and sources for ultrabroadband electro-optic sampling: Experiment and theory, Appl. Phys. Lett. **74**, 1516 (1999).

[41] M. Cornet, J. Degert, E. Abraham, and E. Freysz, Terahertz-field-induced second harmonic generation through Pockels effect in zinc telluride crystal, Opt. Lett. **39**, 5921 (2014).

[42] W.-Q. He, C.-M. Gu, and W.-Z. Shen, Direct evidence of Kerr-like nonlinearity by femtosecond Z-scan technique, Opt. Express **14**, 5476 (2006).

[43] B. Monoszlai, P. S. Nugraha, G. Tóth, G. Polónyi, L. Pálfalvi, L. Nasi, Z. Ollmann, E. J. Rohwer, G. Gäumann, J. Hebling, T. Feurer, and J. A. Fülöp, Measurement of four-photon absorption in GaP and ZnTe semiconductors, Opt. Express **28**, 12352 (2020).

[44] M. Sheik-Bahae, D. J. Hagan, and E. W. Van Stryland, Dispersion and Band-Gap Scaling of the Electronic Kerr Effect in Solids Associated with Two-Photon Absorption, Phys. Rev. Lett. **65**, 96 (1990).